Monthly Notices of the ROYAL ASTRONOMICAL SOCIETY

MNRAS **528,** 2912–2929 (2024) https://doi.org/10.1093/mnras/stad3925
Advance Access publication 2023 December 20

Metal-poor stars observed with the *Magellan Telescope* – IV. Neutron-capture element signatures in 27 main-sequence stars

Mohammad K. Mardini [1,2,3★] Anna Frebel [3,2] Leyatt Betre,[3] Heather Jacobson,[3] John E. Norris[4] and Norbert Christlieb[5]

[1]*Department of Physics, Zarqa University, 13110 Zarqa, Jordan*
[2]*Joint Institute for Nuclear Astrophysics–Center for Evolution of the Elements (JINA-CEE), East Lansing, MI 48824, USA*
[3]*Department of Physics and Kavli Institute for Astrophysics and Space Research, Massachusetts Institute of Technology, Cambridge, MA 02139, USA*
[4]*Research School of Astronomy & Astrophysics, The Australian National University, Weston, ACT 2611, Australia*
[5]*Zentrum für Astronomie der Universität Heidelberg, Landessternwarte, Königstuhl 12, D-69117 Heidelberg, Germany*

Accepted 2023 November 14. Received 2023 October 18; in original form 2023 May 9

ABSTRACT

We present a chemo-dynamical analysis for 27 near main-sequence turnoff metal-poor stars, including 20 stars analysed for the first time. The sample spans a range in [Fe/H] from −2.5 to −3.6, with 44 per cent having [Fe/H]<−2.9. We derived chemical abundances for 17 elements, including strontium and barium. We derive Li abundances for the sample, which are in good agreement with the 'Spite Plateau' value. The lighter elements ($Z < 30$) generally agree well with those of other low-metallicity halo stars. This broadly indicates chemically homogeneous gas at the earliest times. We used the [Sr/Ba] versus [Ba/Fe] diagram to classify metal-poor stars into five populations based on their observed ratios. We find HE 0232 − 3755 to be a likely main *r*-process star, and HE 2214 − 6127 and HE 2332 − 3039 to be limited-*r* stars. CS30302-145, HE 2045 − 5057, and CD −24°17504 plausibly originated in long-disrupted early dwarf galaxies. We also find that the derived [Sr/H] and [Ba/H] values for CD −24°17504 are not inconsistent with the predicted yields of the *s*-process in massive rotating low-metallicity stars models. Further theoretical explorations will be helpful to better understand the earliest mechanisms and time scales of heavy element production for comparison with these and other observational abundance data. Finally, we investigate the orbital histories of our stars. Most display halo-like kinematics although three stars (CS 29504-018, HE 0223 − 2814, and HE 2133 − 0421) appear to be disc-like in nature. This confirms the extragalactic origin for CS 30302-145, HE 2045 − 5057, and, in particular, CD −24°17504 which likely originated from a small accreted stellar system as one of the oldest stars.

Key words: stars: abundances – stars: Population II – Galaxy: halo – early Universe.

1 INTRODUCTION

The chemical evolution of the Galaxy and the early Universe is a key topic in modern astrophysics. By studying the atmospheric composition of the oldest Galactic field metal-poor stars, we can obtain observational constraints on the nature of the nucleosynthetic yields of the first generation(s) of supernovae (SNe) (e.g. Umeda & Nomoto 2002; Keller et al. 2014; Kobayashi et al. 2014), early low-mass star formation processes (Frebel, Johnson & Bromm 2007a; Schneider et al. 2012; Ji, Frebel & Bromm 2014) as well as cosmological models of the first stars and galaxies (e.g. Bromm, Coppi & Larson 2002; Greif et al. 2008; Bromm & Yoshida 2011; Wise et al. 2012), thereby enabling us to reconstruct the physical and chemical conditions of the earliest times. For example, the apparent uniformity in the observed light-element abundances provide important clues to firmly establish what was chemical 'normality' at the earliest times; indicating a well-mixed medium or well-distributed population of similar SNe or both (Cayrel 1996; Cayrel et al. 2004). Also, it provides an indication to what extent individual SNe patterns could have been preserved long enough to allow the formation of metal-poor stars from the ejecta without significant dilution or mixing (e.g. Frebel 2010; Chan & Heger 2017; Mardini et al. 2022a).

In contrast, light neutron-capture elements (e.g. Sr, Y, Zr) spoiled this uniformity by displaying a large abundance spread (reaching nearly 1.5 dex) in comparison with the solar *r*-elements abundance pattern (see figs 5 and 11 in Frebel 2018 and Sneden, Cowan & Gallino 2008). Also, Aoki et al. (2005) showed that stars with high [Sr/Ba] ratios are particularly evident at extremely low metallicity ([Fe/H] < -3.0).[1] In attempt to interpret these observations, Aoki et al. (2005) suggested the weak/limited *r*-process (see also Wanajo et al. 2001; Wanajo & Ishimaru 2005; Izutani, Umeda & Tominaga 2009; Frebel 2018). The limited *r*-process would synthesize the necessary amounts of light neutron-capture elements, including Sr, with little (or no) heavy neutron-capture elements, such as Ba. The

★ E-mail: mardini_mohammad@hotmail.com

[1] $[\mathrm{Fe/H}] = \log_{10}(N_{\mathrm{Fe}}/N_{\mathrm{H}})_{\star} - \log_{10}(N_{\mathrm{Fe}}/N_{\mathrm{H}})_{\odot}$

limited *r*-process has been theoretically studied and associated with massive core-collapse SNe, which is a requirement for the origin of these elements in the most metal-poor stars since type II SNe could have been the only SNe at these early times (e.g. Truran et al. 2002; Travaglio et al. 2004). In addition, Izutani, Umeda & Tominaga (2009) supported this hypothesis by illustrating that massive (25 $M_{\odot}$) energetic hypernovae may produce large amounts of light neutron-capture elements in agreement with values observed in metal-poor stars with large [Sr/Ba] ratios.

Therefore, the [Sr/Ba] ratio is an important diagnostic tool to learn about the nucleosynthetic history that led to the abundance patterns observed in a given star (e.g. McWilliam et al. 1995). However, most available data for these elements are derived from giant stars, which might suffer from internal mixing. In contrast, metal-poor main-sequence stars have shallow convection zones and no internal mixing processes disturbing the stellar atmosphere, and thus these stars would provide the best-preserved chemical record of the early SNe. Considerably more observational time is required to obtain spectra useful for an accurate abundance analysis. Moreover, especially at very low metallicities, spectra with a much higher *Signal-to-noise (S/N)* are required for main-sequence stars to ensure the detection of a sufficiently large number of atomic lines across the spectrum.

Among the first efforts to perform detailed abundance analysis of a large sample of metal-poor main-sequence stars are Carretta et al. (2002), Cohen et al. (2004), and Barklem et al. (2005). Idiosyncratically, the 'First Stars' survey was designed to expand the chemical inventory for extremely metal-poor (EMP; [Fe/H]<-3.0) main-sequence stars (Cayrel et al. 2004). In this work frame, Bonifacio et al. (2007) investigated Li abundances to study the level and constancy of the 'Spite Plateau' at the lowest metallicities. Also, Bonifacio et al. (2009) summarized the differences between the derived atmospheric abundances in various evolutionary statuses. Interestingly, JINAbase (database for metal-poor stars Abohalima & Frebel 2018)[2] shows that only 93 main-sequence stars[3] with [Fe/H]<-3.0 are known to have high-resolution spectroscopic abundance results available. Only 47 per cent of these 93 stars has a metallicity of [Fe/H]<-3.3. Therefore, further explorations of the [Sr/Ba] ratios observed in metal-poor main-sequence stars are desired to robustly characterize the *r*-limited process and gain insight into the (sophisticated) origin of these light neutron-capture elements.

In the era of the Gaia mission (see Gaia Collaboration 2016 for more details about its scientific goals), a more precise picture of the formation and evolution of the Milky Way becomes feasible (for recent review see Helmi 2020). Linking the chemical abundances and kinematics of the most primitive ([Fe/H] <-3.0) stars provides direct insights on the early Galaxy, and by implication, of spiral galaxies in general (Chiti et al. 2021). With the improvements in astrometric measurements reported in the Gaia third data release (hereafter Gaia DR3 Gaia Collaboration 2023) we can further investigate the formation and evolution of the individual Galactic components: thin disc (Mardini et al. 2022a; Hong et al. 2023), the Atari Disc (or metal-weak thick disc e.g. Mardini et al. 2022b), thick disc and halo (e.g. Belokurov et al. 2018; Helmi et al. 2018). However, the bottleneck is to sophistically assign these stars to the various Galactic components. In Mardini et al. (2022b), we developed a sophisticated tool to robustly overcome the aforementioned problem. Employing this technique will not only allow us to investigate the origin of our sample but also to clean up the chemical signature based on the astrophysical formation site(s). Here we caution the reader that using a naive approach (e.g. the height from the disc) would yield some contamination from the other components.

This paper presents results from an ongoing observing program using the *Magellan-Clay* telescope and the MIKE spectrograph at Las Campanas Observatory. The aim is to observe stars with [Fe/H]$\lesssim -3.0$ to discover and characterize the population of metal-poor halo stars. It follows three earlier papers in this series (Placco et al. 2013, 2014a, 2015) on metal-poor giants with and without *s*-process enhancement. The observations of warm metal-poor stars (with no gravity information) also yielded a sample of metal-poor horizontal branch stars which will be presented in a forthcoming paper. The current paper is organized as follows. In Section 2 we describe the selection of the target stars, the observations, and the analysis techniques. In Section 3, information on the stellar parameter determination, abundance analysis, and uncertainties are given. We discuss the abundance results in Section 4. We investigate the observed the chemical signature of the sample with respect to potential nucleosynthetic origins in Section 5 and conclude in Section 6.

2 TARGET SELECTION AND OBSERVATIONS

The target stars in our sample were first observed during several runs between 2007 and 2008 with the Australian National University's 2.3-m telescope/Double Beam Spectrograph combination at the Siding Spring Observatory as part of the program that selects metal-poor candidates (Christlieb et al. 2008) from the Hamburg/ESO objective-prism survey (Wisotzki et al. 1996). The overall scientific goal of this long-term project was the discovery of metal-poor stars having [Fe/H] < -2.0 and the effort lead to the discovery of many new stars with [Fe/H] < -3.5 (e.g. Christlieb et al. 2002; Frebel et al. 2005; Norris et al. 2013; Yong et al. 2013). These medium-resolution spectra have a resolving power of $R \sim 2000$ and cover the wavelength range 3600–5400 Å. The data were reduced with the package FIGARO.[4] Metallicity estimates were determined using the Ca K II line index together with the calibration presented in Beers et al. (1999). All sample stars had [Fe/H] estimates of [Fe/H] $\lesssim -2.8$.

During several runs in 2009, 2010, 2011, and 2014, our sample was then observed with the MIKE spectrograph on the *Magellan-Clay* telescope at Las Campanas Observatory (Bernstein et al. 2003) as part of a large high-resolution spectroscopy follow-up campaign of metal-poor star candidates with [Fe/H] $\lesssim -3.0$. The employed 0.7-arcsec slit width yields a resolving power of $R \sim 35\,000$ in the blue and $\sim 28\,000$ in the red. In only two cases, the 1.0-arcsec slit was used which yields $R \sim 28\,000$ in the $\sim$22 000, respectively. CCD on-chip binning 2 × 2 was always applied. The wavelength coverage of the spectra is $\sim$3400–9000 Å. We observed the well-studied metal-poor star G64-12 (e.g. Carney & Peterson 1981; Frebel et al. 2013; Amarsi et al. 2016; Placco et al. 2016; Giribaldi et al. 2021) as a comparison object and also included CD $-24^{\circ}17504$ (Ryan, Norris & Bessell 1991; Jacobson et al. 2015). Individual exposures, for our program stars, ranged from 5 to 90 min to facilitate cosmic ray removal. The total exposure times ranged from $\sim$10 to 210 min. See Table 1 for more details on the observations.

Reductions of the individual MIKE spectra were carried out using the MIKE Carnegie PYTHON pipeline initially described by Kelson

[2]Compilation available at https://github.com/Mohammad-Mardini/JINAbase.

[3]This number depends on the adopted temperature scales of the individual analyses.

[4]see http://ascl.net/1203.013.

Table 1. Observing details.

Star	α (J2000)	δ (J2000)	B mag	UT date[a]	t_{exp} s	Slit size	v_{rad} km s^{-1}	S/N at 4070 Å[b]	S/N at 5170 Å[b]
CD −24°17504	23 07 20.2	−23 52 36	12.5	2009 July 28	450	0.7	136.4	48	64
CS22188 − 033	00 51 25.9	−38 12 18	13.6	2009 February 05	900	0.7	18.3	15	30
CS29504 − 018	01 32 54.8	−32 55 25	14.1	2009 July 27	800	0.7	− 4.8	37	64
				2009 July 28	1200	0.7	− 5.0		
CS29519 − 133	02 19 22.8	−48 04 38	13.2	2009 July 27	600	0.7	123.5	68	74
CS30302 − 145	19 40 52.2	−48 39 19	14.8	2009 July 27	1500	0.7	196.8	73	93
				2009 July 28	2100	0.7	196.4		
G64 − 12	13 40 02.5	−00 02 19	11.9	2009 Feb 06	400	0.7	443.4	84	137
HE 0219 − 2056	02 21 34.3	−20 42 57	15.7	2009 February 05	3600	0.7	− 46.5	44	70
				2009 February 06	2700	0.7	− 46.4		
				2009 February 07	2700	0.7	− 46.2		
HE 0223 − 2814	02 25 17.0	−28 00 46	13.0	2009 February 07	600	0.7	149.5	51	70
HE 0232 − 3755	02 34 16.4	−37 42 18	13.6	2009 February 07	900	0.7	− 238.1	90	154
HE 0406 − 3120	04 08 31.9	−31 12 58	14.1	2009 February 07	1200	0.7	− 37.8	66	120
				2011 March 11	1800	0.7	− 32.2		
HE 0444 − 2938	04 46 19.6	−29 33 06	15.3	2009 February 05	3600	0.7	247.2	32	55
HE 0526 − 4059	05 28 23.0	−40 56 50	14.7	2010 March 23	3600	1.0	177.4	51	77
HE 1200 − 0009	12 02 53.6	−00 26 20	16.2	2009 February 05	3600	0.7	314.8	58	115
				2009 February 06	5400	0.7	314.6		
				2009 February 07	3600	0.7	314.1		
HE 1214 − 1050	12 16 44.9	−11 06 46	15.5	2009 February 06	3600	0.7	128.9	42	61
				2011 March 10	3000	0.7	100.6		
HE 1245 − 0430	12 47 51.1	−04 46 38	15.5	2009 February 06	3600	0.7	− 189.0	45	60
HE 1309 − 1113	13 11 52.1	−11 29 21	15.3	2009 February 20	2260	0.7	− 43.0	35	52
HE 1401 − 0010	14 04 03.4	−00 24 25	13.9	2010 August 07	1500	1.0	387.4	54	75
HE 1436 − 0654	14 39 36.8	−07 07 47	15.2	2009 July 28	2100	0.7	− 36.2	51	57
				2011 March 13	1800	0.7	− 90.4		
HE 1929 − 6715	19 34 58.3	−67 09 22	14.4	2009 July 28	900	0.7	159.0	75	106
				2010 August 05	1200	0.7	158.1		
HE 2045 − 5057	20 48 46.7	−50 46 29	15.1	2010 August 05	1800	0.7	− 102.3	77	137
				2010 August 06	1200	0.7	− 102.3		
HE 2130 − 4852	21 33 58.9	−48 39 28	15.3	2009 July 27	2000	0.7	− 195.1	86	115
				2010 August 05	2700	0.7	− 201.8		
HE 2133 − 0421	21 36 15.1	−04 08 17	15.9	2010 August 06	3300	0.7	− 2.8	45	86
HE 2141 − 2916	21 44 36.8	−29 02 40	15.1	2009 July 27	2000	0.7	65.0	39	71
HE 2214 − 6127	22 18 16.0	−61 12 17	15.8	2010 August 08	3600	1.0	− 29.3	45	57
HE 2231 − 0635	22 34 07.6	−06 20 00	13.6	2009 July 28	1200	0.7	− 292.1	26	34
HE 2308 − 3543	23 11 32.3	−35 26 42	15.8	2009 July 27	2400	0.7	− 123.9	95	134
				2009 July 28	3300	0.7	− 124.3		
				2010 August 05	1800	0.7	− 124.4		
HE 2332 − 3039	23 35 06.9	−30 22 54	15.6	2010 August 06	2100	0.7	− 12.6	74	89

Notes. [a]At the start of the observation.
[b]*S/N* is given per pixel.

(2003).[5] The wavelength calibration was accomplished using Th-Ar lamp frames. The reduced frames of the stars were normalized using a high-order cubic spline fits to the shape of each echelle order. The overlapping echelle orders were then merged into the final spectra. Two example *S/N* ratio measurements of the final spectra are given in Table 1. Fig. 1 illustrates portions of several stars' spectra around the Sr II line at 4077 Å and the Ba II line at 4554 Å.

To measure the radial velocity (v_{rad}) of each star, we used a cross-correlation technique to match the near-infrared Mg b triplet lines with those of HD140283 which we use as a metal-poor standard star template. For G64 − 12, we measure an average $v_{rad} = 443.4$ km s^{-1}, which is in good agreement with the well-established value of $v_{rad} = 442.5$ km s^{-1} by Latham et al. (2002). The measured RV value for CD −24°17504 also in good agreement with Ishigaki, Chiba & Aoki (2012). Inspection of Table 1 show that four stars have significant radial velocity variations: HE 0406 − 3120, HE 1214 − 1050, HE 1436 − 0654, and HE 2130 − 4852. One additional star, HE 1929 − 6715, shows variance at the ∼1 km s^{-1} level. Excluding the latter as a binary, the fraction of such stars in our sample is 4 of 27 (15 per cent).

[5]Available at https://code.obs.carnegiescience.edu/mike.

3 ABUNDANCE ANALYSIS

3.1 Equivalent width measurements

Equivalent width (EW) measurements are obtained by fitting Gaussian profiles to the lines. See Table 2 for the lines used, their measured equivalent widths and line abundances. Given the low metallicity and warm temperature of our sample stars, only relatively few Fe and other elements lines are available across the entire wavelength range. For example, for iron – having the most lines available of

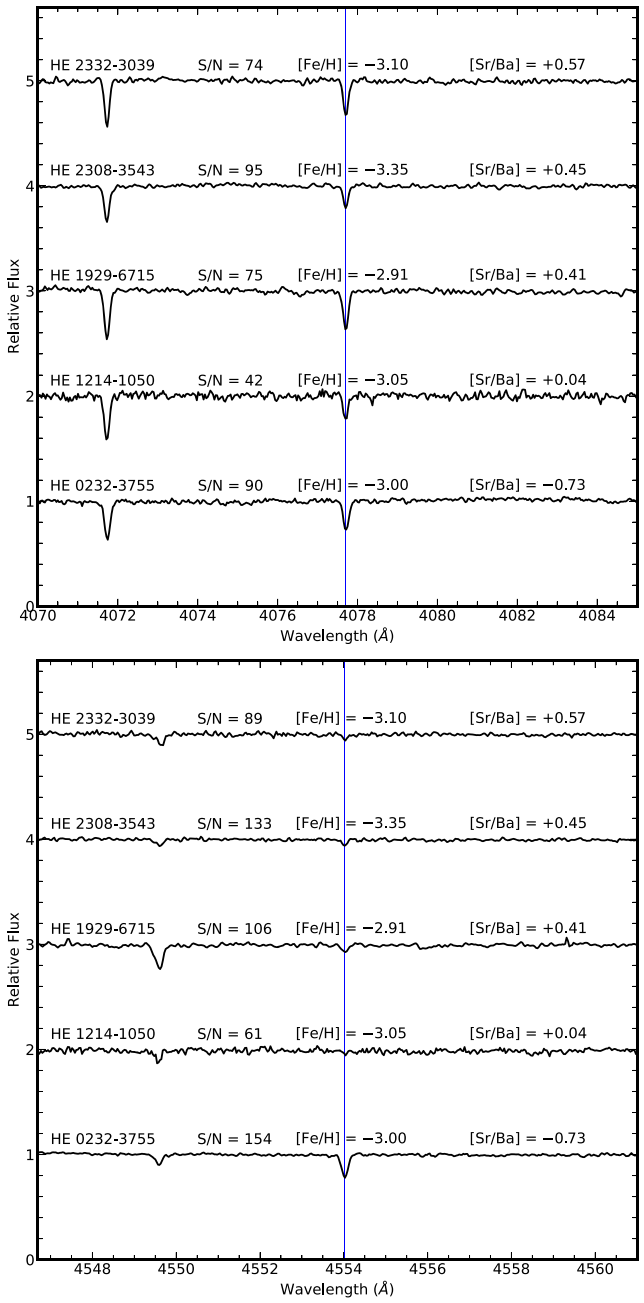

Figure 1. Examples of the spectral region around the Sr II line at 4077 Å (upper) and the Ba II line at 4554 Å (lower), taken from five sample stars with metallicities ranging from [Fe/H] = −2.91 to −3.35. S/N ratios are measured around the feature of interest. [Fe/H] and [Sr/Ba] ratios are listed for illustration.

any element – there are only ∼50–70 Fe I lines available in the blue range, and less than 10 lines in the red spectra. For a few features (Li, CH, Sr, Ba) and upper limits, we use the spectrum synthesis approach. The abundance of a given species is obtained by matching the observed spectrum to a synthetic spectrum of known abundance. Elemental abundances were obtained using the latest version of the MOOG[6] analysis code (Sneden 1973; Sobeck et al. 2011) together with 1D LTE Castelli & Kurucz no-overshoot model atmospheres (Kurucz 1993) and the SMHR software described in Casey (2014).[7]

Fig. 2 compares our equivalent width measurements with those reported in the literature for HE 1401 − 001 (Gull et al. 2021), HE 2308 − 3543 (Roederer et al. 2014b), and G64 − 12 (Matsuno et al. 2017). The upper panels show the one-to-one line (dashed line), the 'best fit' (solid line) through the data, and 10 per cent tolerance (shaded areas). We also listed the solid line equations and the R-squared values in legends. The lower panels show the behaviour of the equivalent widths discrepancies (ΔEW) with wavelength. There is no obvious ΔEW-wavelength correlation. We also listed the mean of ΔEW and standard error (σ) in the legends. In general, the agreement is good, with mean offset $\mu = 1.9$ mÅ (HE 1401 − 001), $\mu = 0.6$ mÅ (HE 2308 − 3543), $\mu = 0.7$ mÅ (G64 − 12). In summary, these ΔEW values represent the varying quality of the spectra (see Table 1).

3.2 Stellar parameters

We used the traditional spectroscopic method and the procedure outlined in Frebel et al. (2013) for stellar parameters determination. We constrain the effective temperatures by plotting the abundances of the measured Fe I lines as a function of their excitation potential ('excitation temperature'). We begin with rough initial temperature guesses according to the shape of the Balmer lines (after visually inspecting them against a set of stars with known temperatures). In general, spectroscopic techniques are known to yield cooler temperatures (and thus, lower surface gravities) than those obtained using photometry. This effect is most pronounced for cool giant stars but much less so for warmer stars near the main-sequence turnoff (see Frebel et al. 2013, for more details). Even though we are dealing with a sample of warm stars, we still apply temperature corrections according to $T_{\rm eff,\,corr} = T_{\rm eff,\,initial} - 0.1 \times T_{\rm eff,\,initial} + 670$, as given in Frebel et al. (2013). We also employed the accurate and precise G, BP and RP magnitudes reported in Gaia Collaboration (2023) to estimate photometric effective temperatures, which are less affected by the inadequacies of the models of stellar atmospheres. We used the best polynomial fit reported by Mucciarelli, Bellazzini & Massari (2021). We estimated the bolometric correction from Casagrande & VandenBerg (2018a, b). The extinction coefficients are calculated from the gird presented in Riello et al. (2021).[8] The resulting $T_{\rm eff,\,corr}$ are in good agreement with those derived from photometry. The uncorrected, corrected spectroscopic, and photometric temperatures are listed in Table 3.

We determine the surface gravity from the ionization equilibrium of Fe I and Fe II abundances. In this iterative process, the microturbulence, $v_{\rm micr}$, is obtained by demanding no trend of individual Fe I line abundances with equivalent widths. The effective temperature uncertainties are estimated to be of the order of 100 K (internal accuracy) and 200 K regarding systematic differences compared with other temperature scales. We estimate the surface gravity uncertainties by searching for the range in gravities in which the Fe II abundance still matches the Fe I abundance within its uncertainties. For an Fe I uncertainty of 0.15 dex this typically results in $\sigma \log(g) = 0.5$ dex. We adopt uncertainties in the micro turbulence of 0.3 km s^{-1} as indicated by the spread of individual line abundances. We also estimate $\log(g)_{\rm Gaia\_plx}$ using corrected parallaxes from the third data release of Gaia (Gaia Collaboration 2023) and equations (2)

[6]Available at https://www.as.utexas.edu/~chris/moog.html.

[7]Available at https://github.com/andycasey/smhr.

[8]For Gaia DR3 are obtained using updated passband and Vega zero points from https://www.cosmos.esa.int/web/gaia/edr3-passbands.

Table 2. Equivalent widths measurements.

El.	λ	χ	log *gf*	EW	log ϵ	EW	log ϵ	EW	log ϵ
				HE 0219 − 2056		HE 1200 − 0009		G64 − 12	
Na I	5889.95	0.00	0.101	34.8	2.80	41.1	2.97	38.2	2.97
Na I	5895.92	...	...	...	...	26.9	3.02	15.2	2.39
Mg I	4703.00	4.34	−0.670	...	...	...	...	8.6	4.91
Mg I	5172.70	2.71	−0.380	78.5	4.48	73.1	4.47	78.9	4.68
Mg I	5183.62	2.72	−0.160	91.4	4.48	84.5	4.43	91.7	4.69
Mg I	5528.40	4.35	−0.490	8.5	4.64	...	...	...	...
Al I	3961.52	0.00	−0.340	45.5	2.75	15.5	2.20	23.1	2.48
Si I	3905.53	1.91	−1.090	79.6	4.63	38.9	4.05	59.8	4.50
Ca I	4226.74	0.00	0.240	86.6	3.18	82.1	3.19	85.7	3.46
Ca I	4302.54	1.90	0.280	8.5	3.16	...	...	18.1	3.65
Ca I	4454.79	1.90	0.260	12.1	3.34	...	...	11.7	3.44
Ca I	5588.76	2.53	0.358	5.8	3.42	...	...	...	...
Ca I	6122.22	1.89	−0.320	4.7	3.41	...	...	...	...
Sc II	4246.82	0.32	0.242	18.3	−0.09	17.1	0.10	17.3	0.12
Ti II	3759.30	0.61	0.270	...	...	56.9	1.59	67.7	1.92
Ti II	3761.33	0.57	0.170	76.4	1.81	47.6	1.49	65.5	1.94
Ti II	3900.54	1.13	−0.450	29.2	2.02	...	...	...	...
Ti II	4012.39	0.57	−1.610	8.5	2.01	...	...	...	...
Ti II	4300.05	1.18	−0.490	18.1	1.80	...	...	18.3	2.03
Ti II	4395.03	1.08	−0.510	29.7	2.00	12.7	1.76	23.2	2.09
Ti II	4399.77	1.24	−1.290	...	...	...	...	5.2	2.26
Ti II	4417.72	1.16	−1.160	...	...	...	...	8.2	2.27
Ti II	4443.81	1.08	−0.700	25.3	2.09	10.3	1.85	13.8	1.99
Ti II	4468.51	1.13	−0.600	16.1	1.79	...	...	18.4	2.08
Ti II	4501.28	1.12	−0.760	24.0	2.15	8.6	1.85	14.4	2.10
Ti II	4533.97	1.24	−0.640	13.4	1.84	14.1	2.08	14.0	2.08
Ti II	4563.77	1.22	−0.820	10.7	1.88	...	...	11.8	2.15
Ti II	4571.98	1.57	−0.340	28.7	2.25	...	...	12.7	2.02
Cr I	4254.33	0.00	−0.110	26.2	2.34	10.6	1.97	15.9	2.25
Cr I	4274.79	0.00	−0.230	...	...	10.8	2.09	18.0	2.43
Cr I	4289.72	0.00	−0.361	11.8	2.17	7.9	2.08	9.5	2.23
Mn I	4030.75	0.00	HFS	syn	<1.80	syn	<1.6	syn	1.60

Note. This table is published in its entirety in the electronic edition of the paper. A portion is shown here for guidance regarding its form and content.

and (3) from Mardini et al. (2019b). The resulting $\log(g)_{\rm corr}$ are in better agreement with those derived from distances. All stellar parameters are summarized in Table 3. We adopted the corrected stellar parameters for the remaining analysis. In summary, our sample stars span a metallicity range of $-3.61 < [Fe/H] < -2.26$.

For inspection of the robustness of the stellar parameters, we overplotted 12 Gyr Dartmouth isochrone with an α-enhancement of $[\alpha/Fe] = 0.4$ and $[Fe/H] = -2.0, -2.5$, and -3.0 (Dotter et al. 2008).[9] We find that our adopted stellar parameters are in good agreement with the isochrones. This is shown in Fig. 3. As can be seen, our sample relatively evenly covers the upper end of the main-sequence, the turnoff region and the subgiant branch. The derived abundances of our sample stars are presented in Table 4. We comment on the individual elemental abundances and their nucleosynthetic origins in Section 4.

3.3 Abundance uncertainties

In Table 4, we list random uncertainties (σ), reflecting the standard deviations of individual line measurements for each element. For abundances measured from only one line, we adopt a nominal uncertainty of 0.10 dex. For abundances measured from two or three lines but with unrealistically small uncertainties, we adopt a nominal value of 0.05 dex. We test the robustness of our derived abundances by changing one stellar parameter at a time by its uncertainty. Table 5 shows the results for all elements, including the random uncertainties. Adding all these error sources in quadrature, the abundances have an overall uncertainty of ∼0.10–0.15 dex. Systematic uncertainties, e.g. arising from the choice of model atmosphere, are not a significant source of error. Uncertainties in *gf* values have not been considered, but are expected to be of minor influence compared with the other uncertainties.

We also compare our stellar parameters and abundance results with those previously obtained for G64 − 12 (Frebel et al. 2013) and CD −24°17504 (Jacobson et al. 2015). Regarding the stellar parameters, temperatures are within 10 K for both stars, although it should be noted that the same spectrum was used in the case of G64 − 12. A difference of 0.01 dex in [Fe/H] was found for G64 − 12, but 0.20 dex for CD −24°17504. This difference is further described in Jacobson et al. (2015) and mostly due to the much higher S/N of their spectrum that enables measurement of additional Fe II lines.

It worth to mention that no abundance uncertainties are not provided by JINAbase, as different authors determine uncertainties in different ways making it impossible to arrive at a homogeneous set of uncertainties. However, all studies included in JINAbase are based on high-resolution spectroscopy of very/extremely metal-poor stars, with most of them having good data quality. Most of the stars

[9] Available at http://stellar.dartmouth.edu/models/index.html.

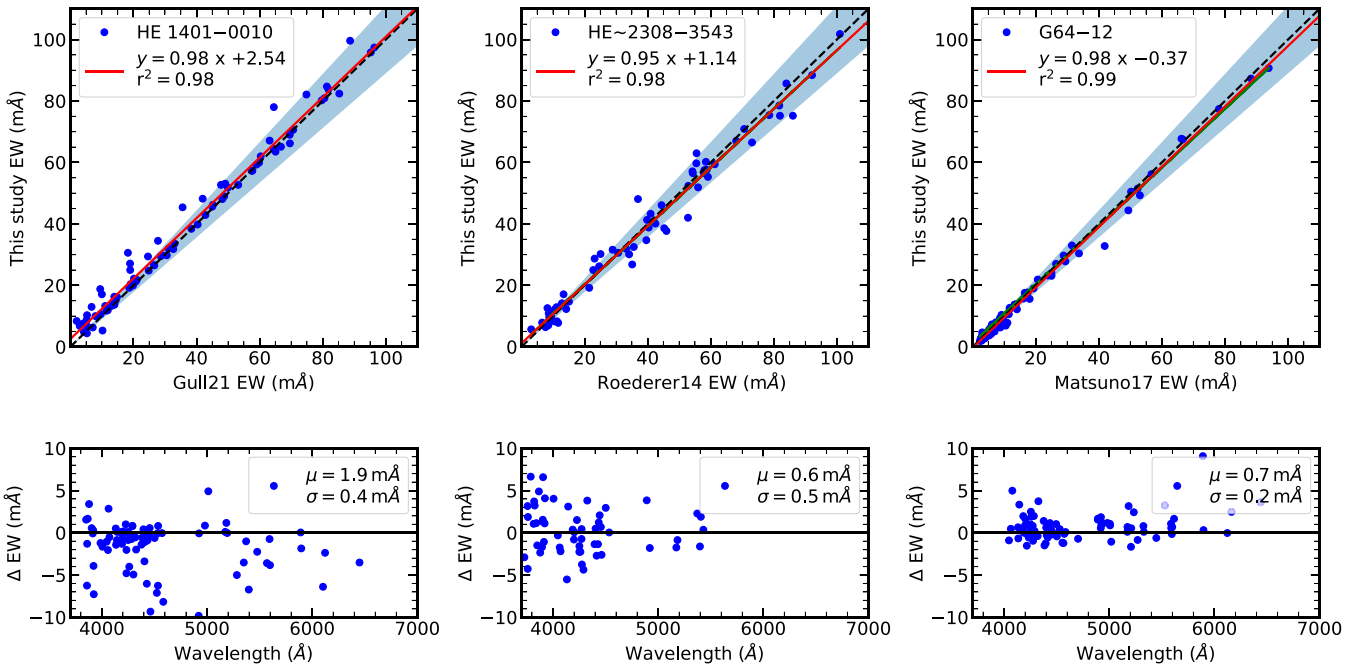

Figure 2. Upper Panels show comparisons of the equivalent widths of HE 1401 − 001 (left), HE 2308 − 3543 (middle), and G64 − 12 (right), with Gull et al. (2021), Roederer et al. (2014b), and Matsuno et al. (2017), respectively. The dashed lines represent one-to-one correlation. The shaded areas represent a 10 per cent tolerance. The solid lines represent best fit through the data. The solid line equations and the R-squared values are listed in the legends. Lower panels show the differences between equivalent widths' measurements (ΔEW) as a function of wavelength. There is no obvious correlation between ΔEW and wavelength. The mean of ΔEW and standard error are listed in the legends.

Table 3. Stellar parameters.

Star	Parallax mass	$T_{\rm eff,\ ini}$ k	log $(g)_{\rm ini}$ dex	[Fe/H]$_{\rm ini}$ dex	$v_{\rm micr,\ ini}$ [km s^{-1}]	$T_{\rm eff,\ corr}$ k	log $(g)_{\rm corr}$ dex	[Fe/H]$_{\rm corr}$ dex	$v_{\rm micr,\ corr}$ [km s^{-1}]	$T_{\rm eff,\ BP\text{-}G}$ k	log$(g)_{\rm Gaia_plx}$ dex
CS22188 − 033	2.2185	6200	4.40	−2.65	1.45	6250	4.50	−2.60	1.45	6265	4.45
CS29504 − 018	1.2439	6240	3.70	−2.75	1.75	6286	3.75	−2.70	1.80	6387	4.01
CS29519 − 133	1.7982	6050	3.50	−2.70	1.45	6115	3.75	−2.65	1.40	6187	4.07
CS30302 − 145	0.8697	6220	3.60	−2.95	1.70	6268	3.75	−2.95	1.70	6390	3.90
HE 0219 − 2056	0.5171	6569	4.15	−2.95	1.55	6582	4.20	−3.16	1.55	6487	3.99
HE 0223 − 2814	1.5857	6180	3.45	−2.55	1.65	6232	3.70	−2.50	1.65	6228	3.95
HE 0232 − 3755	2.2784	6140	4.35	−3.05	1.45	6196	4.40	−3.05	1.50	6292	4.46
HE 0406 − 3120	0.9404	6490	4.20	−2.65	1.40	6511	4.20	−2.65	1.40	6373	3.95
HE 0444 − 2938	0.4985	6390	4.05	−2.60	1.75	6421	4.00	−2.55	1.80	...	...
HE 0526 − 4059	0.9729	6150	3.70	−3.15	1.50	6205	3.75	−3.38	1.55	6319	3.95
HE 1200 − 0009	0.4905	6430	4.00	−3.46	1.65	6457	4.05	−3.42	1.65	6338	4.13
HE 1214 − 1050	0.9641	5900	3.80	−2.95	1.35	5980	3.80	−3.05	1.40	6080	3.95
HE 1245 − 0430	0.6825	6250	3.50	−2.85	1.35	6295	3.80	−2.85	1.35	6466	4.07
HE 1309 − 1113	0.5645	6350	3.85	−2.50	1.55	6385	3.90	−2.76	1.55	6431	4.04
HE 1401 − 0010	1.3259	6160	3.35	−2.60	1.75	6214	3.75	−2.60	1.70	6245	4.00
HE 1436 − 0654	0.7478	6140	3.55	−2.70	1.70	6196	3.85	−2.65	1.70	6336	4.02
HE 1929 − 6715	1.4456	6050	3.60	−2.70	1.35	6115	3.65	−2.91	1.35	6236	3.75
HE 2045 − 5057	0.9949	6145	3.75	−2.40	1.30	6200	3.85	−2.63	1.35	6266	3.90
HE 2130 − 4852	0.4207	5760	3.50	−2.90	1.45	5854	3.65	−2.85	1.50	5833	3.57
HE 2133 − 0421	0.7855	6000	3.70	−2.85	1.45	6070	3.70	−2.80	1.50	6106	3.82
HE 2141 − 2916	0.3798	5940	3.50	−2.88	1.50	6016	3.60	−2.82	1.55	6096	3.65
HE 2214 − 6127	0.4160	5540	3.15	−3.10	1.60	5656	3.55	−3.00	1.60	5726	3.53
HE 2231 − 0635	0.4519	6350	3.90	−2.31	1.35	6385	3.95	−2.26	1.35	6391	4.07
HE 2308 − 3543	1.0997	5930	4.45	−3.66	1.30	6007	4.60	−3.61	1.30	6091	4.48
HE 2332 − 3039	1.1734	5940	3.85	−3.43	1.45	6016	3.85	−3.35	1.45	6102	3.85
CD −24°17504	3.1957	6210	3.60	−3.26	1.35	6259	3.80	−3.23	1.35	6370	3.90
G64 − 12	3.6494	6440	4.25	−3.32	1.30	6466	4.25	−3.27	1.35	6411	4.21

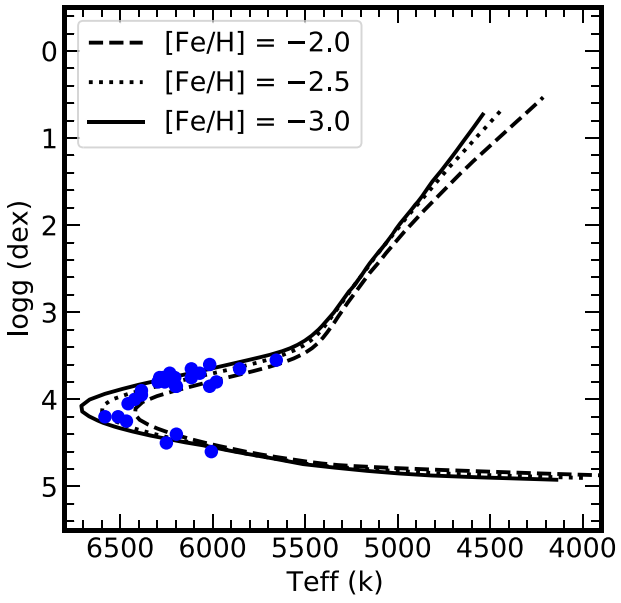

Figure 3. Adopted surface gravity ($\log(g)_{\rm corr}$) as a function of effective temperature ($T_{\rm eff,\,corr}$) of our sample stars in comparison with 12 Gyr isochrones with metallicities ranging from [Fe/H] = −2.0 to −3.0.

are cool(er) red giants. Accordingly, uncertainties arising from such studies are typically around 0.1–0.2 dex for Sr and Ba, not unlike what we find for our main-sequence stars.

4 CHEMICAL ABUNDANCE SIGNATURES OF 27 NEAR MAIN SEQUENCE TURNOFF STARS

4.1 Lithium

As stars evolve from the main sequence towards the red giant branch, their surface convection zone deepens. The deeper layers towards the bottom of the convection zone are hot enough to destroy the fragile

Table 5. Example abundance uncertainties.

Elem.	Random error	$\Delta T_{\rm eff}$ + 150 K	$\Delta\log g$ +0.5 dex	$\Delta v_{\rm micr}$ + 0.3 km s^{-1}	Total σ
		G64 − 12			
O I					
Na I		− 0.10	− 0.01	− 0.02	0.10
Mg I		− 0.08	− 0.02	− 0.02	0.08
Al I		− 0.11	0.00	− 0.01	0.11
Si I		− 0.11	− 0.01	− 0.04	0.12
Ca I		− 0.08	− 0.01	− 0.01	0.08
Sc II		− 0.07	0.09	0.00	0.11
Ti I		− 0.13	0.00	− 0.01	0.13
Ti II		− 0.08	0.09	− 0.04	0.13
Cr I		− 0.13	0.00	0.00	0.13
Cr II		− 0.06	0.08	− 0.01	0.10
Mn I		− 0.14	0.01	0.00	0.14
Fe I		− 0.12	− 0.01	− 0.03	0.12
Fe II		− 0.02	0.00	− 0.01	0.02
Co I		− 0.13	0.01	− 0.01	0.13
Ni I		− 0.17	− 0.02	− 0.06	0.18
Sr II		− 0.09	0.08	− 0.08	0.14
Ba II		− 0.10	0.09	0.00	0.13
		CS29519 − 133			
Na I		0.10	− 0.02	− 0.03	0.11
Mg I		0.09	− 0.07	− 0.03	0.12
Al I		0.12	0.00	− 0.01	0.12
Si I		0.13	− 0.06	− 0.08	0.16
K I		0.09	0.00	0.00	0.09
Ca I		0.08	− 0.02	− 0.02	0.08
Ca II		0.00	0.00	0.00	0.00
Sc II		0.08	0.10	− 0.01	0.13
Ti I		0.14	0.00	− 0.01	0.14
Ti II		0.08	0.08	− 0.05	0.12
V I		0.10	0.00	0.00	0.10
Cr I		0.15	− 0.02	− 0.04	0.16
Mn I		0.16	0.00	0.00	0.16
Fe I		0.13	− 0.02	− 0.05	0.14
Fe II		0.03	0.10	− 0.01	0.10
Co I		0.15	0.00	0.00	0.15
Ni I		0.19	− 0.05	− 0.07	0.21
Sr II		0.08	0.08	− 0.09	0.14
Ba II		0.11	0.09	0.00	0.14

Table 4. *Magellan*/MIKE abundances.

	HE 0219 − 2056					HE 1200 − 0009					G64 − 12				
Elem.	lg ϵ(X)	[X/H]	[X/Fe]	σ	N	lg ϵ(X)	[X/H]	[X/Fe]	σ	N	lg ϵ(X)	[X/H]	[X/Fe]	σ	N
Li I	2.14	...	...	0.10	1	2.16	...	...	0.10	1	2.19	...	...	0.10	1
C (CH)	7.02	−1.41	<1.75	...	1	6.41	−2.02	<1.40	...	1	6.54	−1.89	1.38	0.10	1
Na I	2.68	−3.56	− 0.40	0.20	2	2.94	−3.30	0.12	0.07	2	2.97	−3.27	0.00	0.10	2
Mg I	4.86	−2.74	0.42	0.12	4	4.37	−3.23	0.19	0.10	6	4.74	−2.86	0.41	0.12	7
Al I	2.62	−3.83	− 0.67	0.10	1	2.32	−4.13	− 0.71	0.05	3	2.47	−3.98	− 0.71	0.10	1
Si I	4.30	−3.21	− 0.05	0.10	1	4.08	−3.43	− 0.01	0.10	1	4.42	−3.09	0.18	0.10	1
Ca I	3.67	−2.67	0.49	0.13	3	3.55	−2.79	0.63	0.19	8	3.56	−2.78	0.49	0.12	12
Sc II	0.57	−2.58	0.58	0.10	1	− 0.56	−3.71	− 0.29	0.10	1	0.12	−3.03	0.24	0.15	2
Ti I	2.17	−2.78	0.38	0.10	1	1.97	−2.64	0.47	0.21	2	2.34	−2.61	0.66	0.11	3
Ti II	2.32	−2.63	0.53	0.09	11	2.14	−2.81	0.61	0.12	16	2.12	−2.83	0.44	0.11	22
Cr I	2.39	−3.25	− 0.09	0.11	3	3.64	−3.60	− 0.18	0.07	3	2.14	−3.50	− 0.23	0.13	6
Mn I	...	...	...	...	...	...	...	...	...	...	1.54	−3.89	− 0.62	0.05	3
Fe I	4.34	−3.16	...	0.14	44	4.08	−3.42	...	0.11	35	4.23	−3.27	...	0.05	76
Fe II	4.35	−3.15	− 0.01	0.06	2	4.06	−3.44	− 0.02	0.08	2	4.22	−3.28	− 0.01	0.05	5
Co I	...	...	...	...	...	0.93	−3.06	0.36	0.10	1	2.43	−2.56	0.71	0.10	1
Ni II	3.35	−2.87	0.29	0.06	2	3.02	−3.20	0.22	0.11	6	3.04	−3.18	0.09	0.10	10
Sr II	− 0.58	−3.45	− 0.30	0.05	2	− 0.90	−3.77	− 0.35	0.13	2	0.03	−2.84	0.43	0.06	2
Ba II	− 1.06	−3.24	− 0.09	0.16	2	− 1.07	−3.25	0.17	0.05	2	− 0.92	−3.10	0.17	0.05	2

Note. This table is published in its entirety in the electronic edition of the paper. A portion is shown here for guidance regarding its form and content.

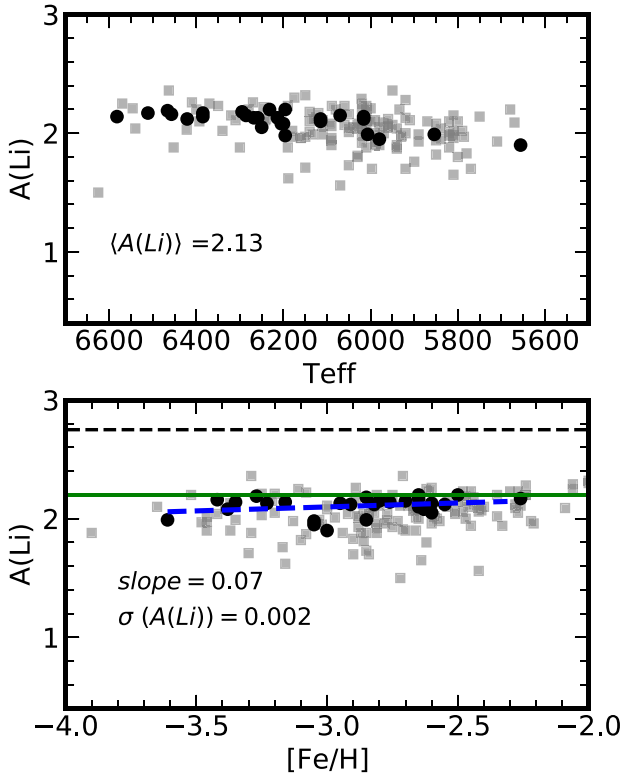

Figure 4. Lithium abundances A(Li) for our sample of stars (black points); as a function of effective temperature (top panel) and metallicity [Fe/H] (bottom panel). Grey squares represent dwarf stars ($5500 < T_{\rm eff} < 6700$, $\log(g) > 3.5$, and [Fe/H]<-1.5) selected from JINAbase. The solid green line represents the 'Spite plateau' A(Li) $= 2.23$. Dashed black lines represent the primordial lithium A(Li) $= 2.72$. Dashed blue line represents the 'best-fitting' line through the data. The slope and residual are listed. Our sample has a mean lithium abundance of A(Li) $= 2.13$.

element lithium (Deliyannis, Demarque & Kawaler 1990). Typical main-sequence Galactic stars have Li abundances of $A(^7\mathrm{Li}) \sim 2.2$ (Spite & Spite 1982). Given the evolutionary status of our sample, we detected the Li I doublet at 6707 Å in all of our spectra. We considered the Hyperfine splitting (HFS) effect and multiple isotopes in the syntheses of Li. The derived abundances are listed in Table 4. In Fig. 4, we show $A(^7\mathrm{Li})$ abundances as a function of effective temperature (upper panel) as well as [Fe/H] (lower panel). We also selected similar dwarf stars ($5500 < T_{\rm eff} < 6700$, $\log(g) > 3.5$, and [Fe/H]<-2.0) from JINAbase for comparison. We also plot the primordial lithium $A(^7\mathrm{Li}) = 2.75$ (dashed black line) and our linear 'best-fitting' line (dashed blue line).

In general, our abundances are in good agreement with those found in the other dwarfs at the 'Spite plateau' (green solid line) although at a somewhat lower mean value of A(Li) $= 2.13$ (from stars with $6050 < T_{\rm eff} < 6600$). Norris et al. (2023) extensively investigated the behaviour of A(Li) as a function of $T_{\rm eff}$, [Fe/H], and [C/Fe]. Reanalysing literature data for warm metal-poor dwarfs, they reconfirmed the 'meltdown' of the Spite plateau (Bonifacio et al. 2007) in the metallicity range of $-4.2 <$ [Fe/H] < -3.0. While we find relatively flat trend for our warmest stars, our most metal-poor star (HE 2308 − 3543 with $T_{\rm eff} = 6007$ K) has A(Li) $= 2.0$ which adds to stars with sub-Spite Plateau abundances.

4.2 Light elements: carbon through zinc

Fig. 5 shows the abundance results [X/Fe] as a function of metallicity [Fe/H] in comparison with other very metal-poor ([Fe/H]$\lesssim -2.0$) stars collected by JINAbase from the literature (Abohalima & Frebel 2018). Error bars depict representative uncertainties (± 0.15 dex) of each element for our sample as well as the JINAbase data set. Due to the low metallicity and the warm effective temperature of all sample stars, carbon measurements were only possible in 15 of 27 stars. For these 15 stars, when possible, we used the molecular G-band head at 4313 Å for deriving A(C). In a few cases, the feature at 4323 Å was also used. For stars with no C detection, we derived upper limits which are rather high (between [C/Fe] ~ 0.5 and 1.5) and unfortunately not very meaningful. 12 of the 15 stars with C detection have [C/Fe] > 0.7 while four have [C/Fe] > 1.0. Furthermore, there is a tendency for the most metal-poor stars to have the higher [C/Fe] values, as can be seen in Fig. 5. Assuming that all stars with upper limits are not carbon-enhanced, the fraction of carbon-enhanced metal-poor stars in this sample would be 44 per cent. This number would only increase if any other stars with upper limits would also be carbon-enhanced. A fraction of ~ 44 per cent, taking into account the [Fe/H] distribution of the sample, is in good agreement with the results of Placco et al. (2014b). They established the fraction of carbon-enhanced metal-poor stars in the halo; 24 per cent for stars with [Fe/H] ~ -2.0 and 43 per cent for stars with [Fe/H] ~ -3.3 (see their fig. 9).

We measure a suite of light-, α- and Fe-peak elements: Na, Mg, Al, Si, Ca, Sc, Ti, Cr, Mn, Co, Fe, and Ni. Detailed comments on the elements and employed lines can be found in Frebel et al. (2007b) and will not be repeated here. In Fig. 5, we compare our results with those of other metal-poor stars collected by JINAbase. Regarding these light elements ($Z < 26$), all stars share very similar abundance ratios, [X/Fe], and appear to be typical halo stars. Only CS 30302 − 145 appears to have low [Mg, Ca/Fe] ratios, HE 1200 − 0009 and HE 0526 − 4059 have high low [Sc/Fe] ratio, and HE 1214 − 1050 has relatively low [Al, Sc, Ti/Fe].

Cayrel et al. (2004) noted that, especially at the lowest metallicities (in the range $-4.0 \lesssim$ [Fe/H] $\lesssim -3.0$), there is little scatter in the data indicating a chemically homogeneous medium already at the earliest times. The halo-typical abundances in our ten main-sequence stars at [Fe/H] ~ -3.0 are in line with this finding and furthermore support that there was a population of extremely metal-poor stars that formed from a medium enriched in light elements originating from the same process(es) and in similar quantities and elemental distributions. There are, however, also other stars (e.g. McWilliam et al. 1995; Aoki et al. 2002) that significantly deviate from the general halo trends as found among the lighter elements. Below [Fe/H] ~ -3.5 the fraction of these 'outliers' is around 20–30 per cent, but none of our stars shows such behaviour.

4.3 Neutron-capture elements

Very few neutron-capture elements are measured for turnoff stars because their spectral lines are generally very weak. Unsurprisingly, we only detect two Sr II lines at λ4077 and λ4215 and two Ba II lines at 4554 Å and 4934 Å in our stars (see Fig. 1 for some examples). No other lines for neutron-capture elements were detected. HFS effects were taken into account when determining abundances from the Ba lines. The measured [Sr/Fe] ratio in our target stars ranges from -1.52 to $+0.43$ dex. The [Ba/Fe] ratio ranges from -0.92 to $+0.69$ dex. Fig. 5 shows principal agreement between the measured ratios ([Sr/Fe] and [Ba/Fe]) for our sample stars and those of literature

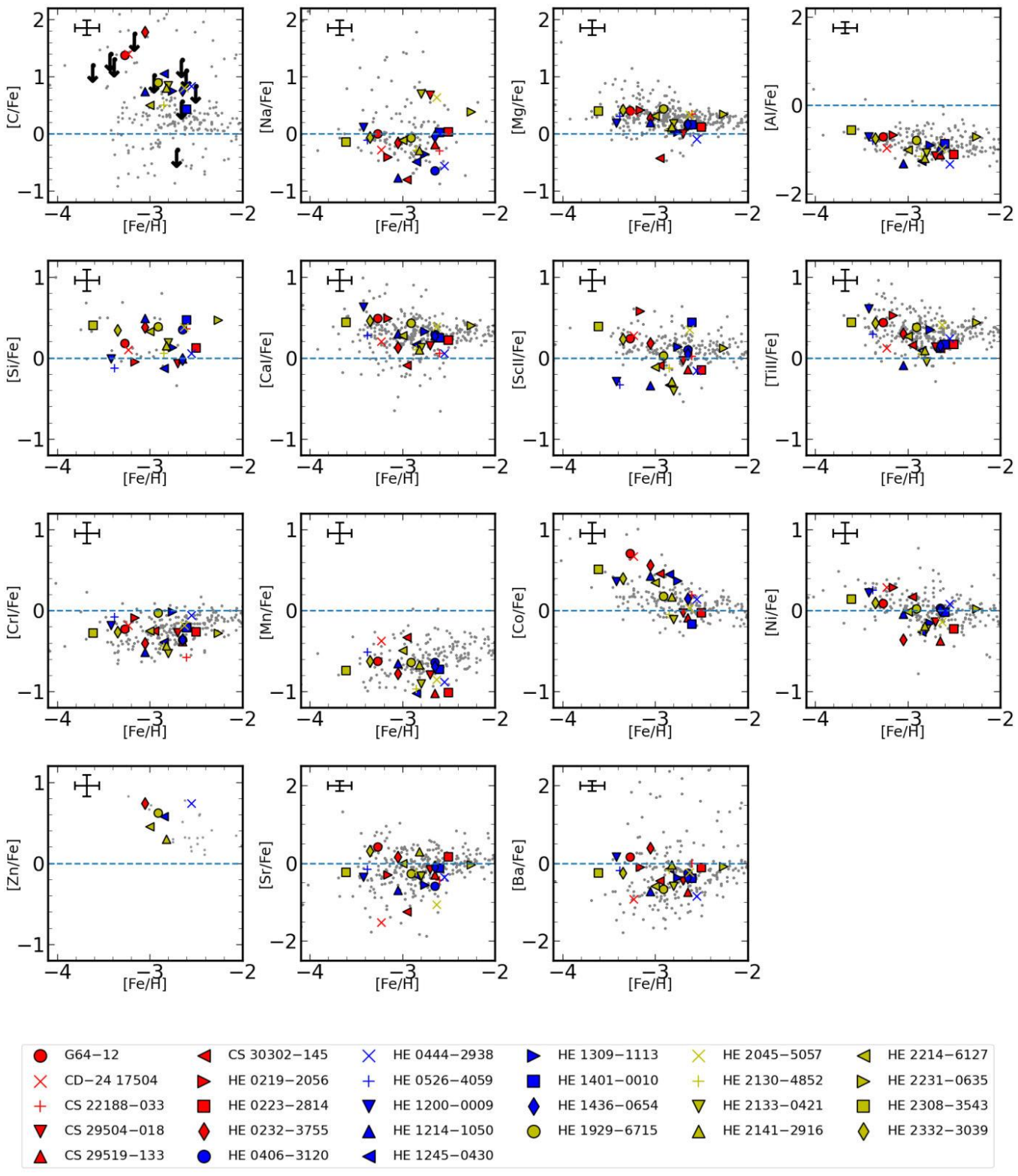

Figure 5. Abundance ratios as a function of metallicity of our metal-poor stars (various symbols) and literature stars collected by JINAbase (Abohalima & Frebel 2018). Error bars depict representative uncertainties (±0.15 dex) of each element for our sample as well as the JINAbase data set. Data taken from: Cayrel et al. (2004); Roederer et al. (2014a); Barklem et al. (2005); Yong et al. (2013); Aoki et al. (2013); Jacobson et al. (2015); Mardini et al. (2019a, b, 2020).

stars, as collected by JINAbase. However, the overall abundance uniformity among the lighter elements does not hold for the neutron-capture elements which display a rather large star-to-star scatter, particularly at the lowest metallicities (e.g. Frebel 2018).

In the literature, barium (Z = 56 mainly produced by the *s*-process) and europium (Z = 63 mainly produced by the *r*-process; see table 3 in Prantzos et al. 2020) are usually used as a quick tool to identify the underlying production mechanisms of the observed neutron-capture

elements (see table 1 in Frebel 2018). Unfortunately, we could not derive any A(Eu) for our sample. Therefore, we could not use these classical abundance criteria to gain putative insight into the chemical enrichment of our stars. However, in Section 5.1, we show that the location of a star in the [Sr/Ba]-[Ba/Fe] space can be also used to comment on its possible chemical enrichment.

5 DISCUSSION

5.1 Exploring the origins of neutron-capture elements

The synthesis of the majority of elements with Z >30 is possible only through neutron-capture reactions when neutrons overcome the Coulomb barrier. The two neutron-capture (*s*- and *r*-) processes can be separated based on the time-scales of the neutron-capture and associated β-decay. The *s*-process denotes that the neutron-capture is slower than the time-scale of the β-decay of the nucleus involved. Nuclei along the so-called 'valley of β-stability' are synthesized this way. In comparison, the *r*-process happens in more violent events and thus rapidly synthesize large amounts of unstable/radioactive nuclei far from stability (e.g. Meyer 1994).

We now explore the origins of the observed neutron-capture elements by means of the [Sr/Ba] versus [Ba/Fe] behaviour in our stars to better understand the formation environment in which these nuclei formed. In Fig. 6, we compare our results ([Sr/H,Fe]; left panels, [Ba/H,Fe]; middle panels, and [Sr/Ba]; right panels) as a function of [Fe/H] with the body of data of Galactic metal-poor stars collected by the JINAbase (small grey circles). We also selected all JINAbase stars which have Sr, Ba, and Eu measurements. The resulting sample contains 1069 distinct stars (shown with various symbols). Black squares represent our sample stars.

In Fig. 6, we plot all stars collected by JINAbase on the background (small grey circles) and then overplot stars with Sr, Ba, and Eu measurements. For the latter ones, we use the classes and signatures of metal-poor stars presented in Table 1 in Frebel (2018) to label their possible chemical signature. We begin by selecting orange diamonds (100 data points) which represent the strongly enhanced *r*-process stars with [Eu/Fe] >+0.7 and [Ba/Eu] <0.0. Cyan asterisks represents mildly enhanced *r*-process stars (397 data points; +0.3 < [Eu/Fe] <+0.7 and [Ba/Eu] <0.0). Blue crosses represent *s*-process rich stars (40 data points; [Ba/Fe] >+1.0 and [Ba/Eu] >+0.5). Green triangles represent limited *r*-process stars (92 data points; [Eu/Fe] <0.3, [Sr/Ba] >0.5, and [Sr/Eu] >0.0). Pink plus-symbols represents the remaining metal-poor (440 data points; neutron-capture normal) stars after subtracting out all the aforementioned signatures and classes. We also add ultra-faint dwarf (UFD) galaxy stars (red filled circles).[10]

Fig. 6(a) and (b) show the observed [Sr/Fe] and [Ba/Fe] as a function of [Fe/H]. No clear trend for metallicity can be observed. However, the most metal-poor ([Fe/H] <−3.0) stars seems to have the lower [Sr/Fe] and [Ba/Fe] values compared to the more metal-rich ones. This could be a direct sign for an early chemical enrichment. The production of the heavy elements occurred later in the Galaxy, because the *s*- and *r*-processes need seed nuclei (e.g. iron). Fig. 6(d) and (e) reveal a similar early chemical enrichment signature but a clear correlations between [Sr, Ba/H] and [Fe/H] are seen.

Fig. 6(f) shows [Sr/Ba] as a function of [Fe/H]. Interestingly, the [Sr/Ba] values, for all stars, are enveloped in the range of −2.5 < [Sr/Ba] <2.5. The upper limit of this range reflect −1.5 − [Fe/H] of the lower limit of the [Fe/H] (i.e. −4). The lower limit of this range reflect −1.5 + [Fe/H] of the upper limit of the [Fe/H] (i.e. −1). At lower metallicity, obvious scatter in the [Sr/Ba] values is clearly seen. This scatter might reflect the production of Ba by the *r*-process. For clarity, individual error bars are not added, but we show a representative error bar of ±0.15 dex in the upper right corner of each panel. In addition, we note that any such inhomogeneities would largely cancel out for a [Sr/Ba] ratio (but less so for [X/Fe]). Accordingly, and since we used mainly the [Sr/Ba] for our classifications, we do not add any error bar for the [Sr/Ba] ratio.

The dashed line in Fig. 6(c) denotes [Sr/Ba] = − [Ba/Fe] − 0.50, which separates the regions populated by UFD stars from other Galactic metal-poor stars. Excluding Reticulum II stars (Ji et al. 2016a), the [Sr/Ba] ratio of the stars in the UFD galaxies region strongly depends on their [Ba/Fe] ratio and could be a signature of the earliest star-forming clouds (Frebel & Norris 2015). Regarding the [Sr/Ba] ratio for Galactic metal-poor stars, we find four features (i) the main *s*-process stars are wildly dispersed (∼2 dex) for a given [Ba/Fe] and have the lowest [Sr/Ba] values; (ii) the limited *r*-process stars show significant scatter (∼1 dex) in [Sr/Ba] and have the highest [Sr/Ba] values; (iii) the strong *r*-process stars also shows significant scatter in [Sr/Ba] and bridge the gap between the *s*-process and limited *r*-process stars; (iv) the mild *r*-process stars and neutron-capture normal stars significantly overlap and are centred at [Sr/Ba] = 0.0 and [Ba/Fe] = 0.0. No apparent separation can be easily found.

Based on the bulk of each population, we suggest new abundance criteria to differentiate between the origins of neutron-capture enhancements. The observed neutron-capture elements in metal-poor stars with [Sr/Ba] >0.6 and [Ba/Fe] <0.0 are most likely synthesized by the limited *r*-process. The neutron-capture elements observed in stars with [Sr/Ba] <−0.6 and [Ba/Fe] >1.5 were formed in a weak neutron flux environment associated with the main *s*-process. Stars with −0.4 < [Sr/Ba] <0.4 and 0.0 < [Ba/Fe] <1.0 might have chemical signatures associated with the population of *r*-II stars. Stars with −0.2 < [Sr/Ba] <0.6 and [Ba/Fe] <0.0 are most likely mild *r*-process star or are 'neutron-capture normal', i.e. show no enhancement in neutron-capture elements.

Using the aforementioned abundance criteria, we find no stars with strong (external) *s*-process enrichment in our sample. Instead, the vast majority of our sample stars are most likely *r*-I and/or neutron-capture normal stars given their position in the [Sr/Ba] versus [Ba/Fe] diagram, i.e. they are mildy enhanced, or not enhanced in neutron-capture elements beyond the solar ratio. The exceptions are (1) HE 0232 − 3755 which is most likely an *r*-II star given its [Sr/Ba] ratio; (2) HE 2214 − 6127 and HE 2332 − 3039 which are most likely limited-*r* stars (further discussed below); and (3) CS 30302-145, HE 2045 − 5057, and CD −24°17504 which reside below the main trend of [Sr/Ba] versus [Ba/Fe] as set by Galactic metal-poor stars (dashed line), in the region that is characteristically populated by UFDs stars, see Fig. 6. They may likely have a separate origin as further discussed below.

We note that regardless of their neutron-capture abundance levels, while the production mechanisms (and sites) of lighter elements ($Z <$ 30) and (any) neutron-capture elements in SNe would be decoupled, we here assume that if a SN that produced any neutron-capture elements it would also generate lighter elements in somewhat 'standard' quantities (Woosley & Weaver 1995). As such, a massive progenitor exploding as a SN would also provide α-element abundances at the typical + 0.3–0.4 dex level. Since the individual Sr and Ba abundances, and also [Fe/H], are relatively low for most of our

[10]Compilation available at https://github.com/alexji/alexmods/blob/master/alexmods/data/abundance_tables/dwarf_lit_all.tab.

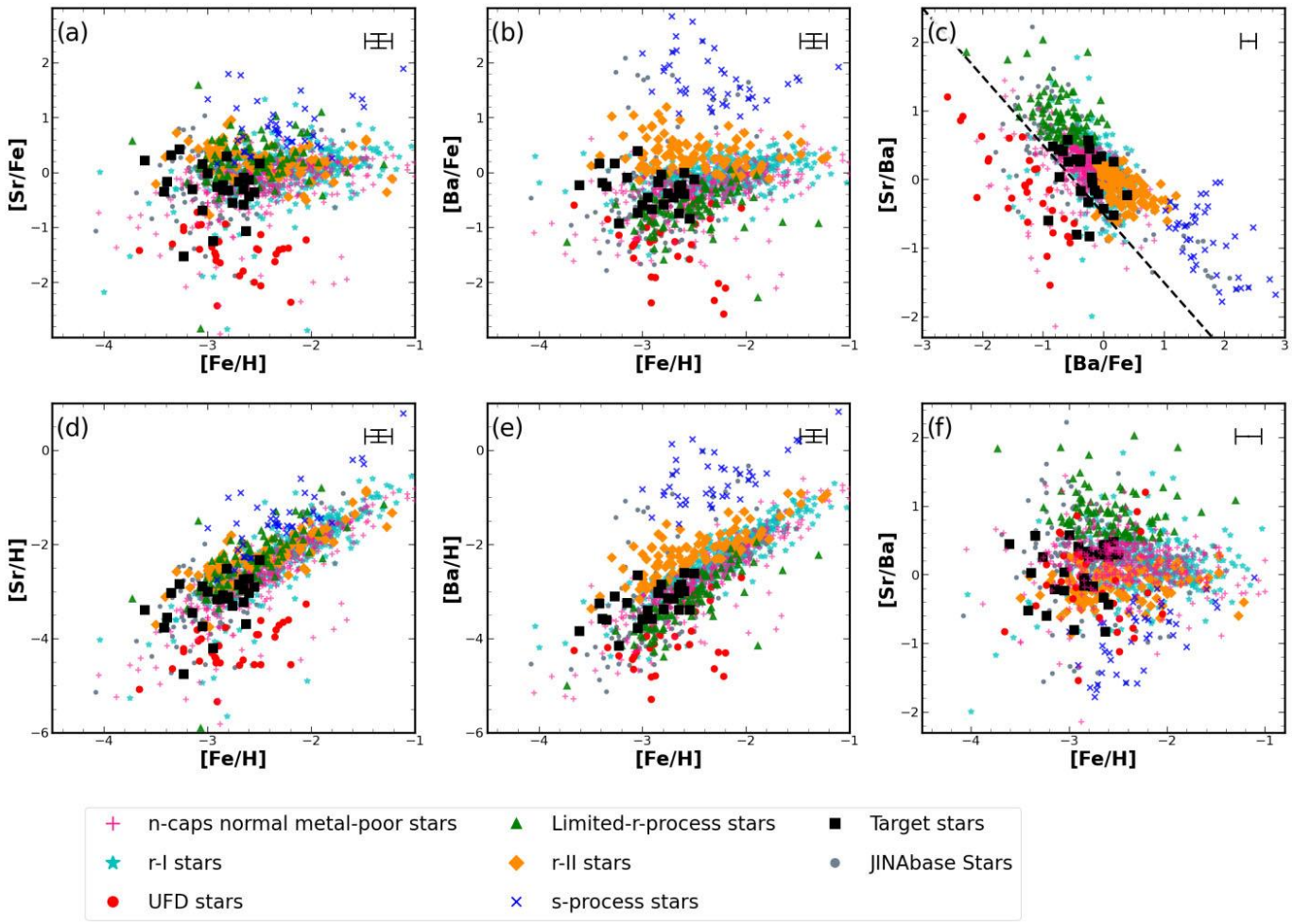

Figure 6. Sr and Ba abundances for our sample stars in comparison with literature metal-poor stars. Cyan asterisks represent r-I stars. Green triangles represent limited *r*-process stars. Pink plus-symbols represent the neutron-capture normal metal-poor stars. Black squares represent our sample stars. Red circles represent ultra-faint dwarf galaxy stars. Orange diamonds represent main *r*-process stars. Blue crosses represent *s*-process stars. As can be seen there is a separation of these populations in the [Sr/Ba] versus [Ba/Fe] space which helps to distinguish the origins of the chemical signatures of metal-poor stars. For clarity, individual error bars are not added, but we show a representative error bar of ±0.15 dex in the upper right corner of each panel. Metal-poor stars data taken from: Roederer et al. (2014a); Barklem et al. (2005); Ryan, Norris & Bessell (1991); Cohen et al. (2004); Hollek et al. (2011); Bonifacio et al. (2012); Mardini et al. (2019a); Aguado et al. (2017a); Mardini et al. (2019b); Yong et al. (2013); Frebel et al. (2010); Hansen et al. (2015); Mardini et al. (2020); Jacobson et al. (2015); Ezzeddine et al. (2019); Spite et al. (2014); Cayrel et al. (2004); Norris et al. (2007); Mardini et al. (2019c); Aguado et al. (2021); Lai et al. (2004); Almusleh et al. (2021); Placco et al. (2020); Ryan, Norris & Beers (1996); Aguado et al. (2018); Taani et al. (2019a); Taani, Abushattal & Mardini (2019b); Aoki et al. (2007); Aoki et al. (2013); Cohen et al. (2013); Honda et al. (2011); Lai et al. (2008); Casey & Schlaufman (2015); Li et al. (2015c); Masseron et al. (2006); Rich & Boesgaard (2009); Taani, Vallejo & Abu-Saleem (2022); Ryan, Norris & Beers (1999); Spite et al. (1999); Depagne et al. (2000); Spite et al. (2000); Sivarani et al. (2006); Norris, Ryan & Beers (2001); Placco et al. (2014a); Caffau et al. (2011b); Frebel et al. (2005); Frebel et al. (2008); Li et al. (2015a); Behara et al. (2010); Caffau et al. (2011a); Susmitha Rani et al. (2016); Aguado et al. (2017b); Carretta et al. (2002); For & Sneden (2010); Li et al. (2015b); Keller et al. (2014); Frebel et al. (2015); Caffau et al. (2013); Plez & Cohen (2005); Christlieb et al. (2002); Frebel et al. (2019). UFDs stars data taken from: Koch et al. (2008); Simon et al. (2010); Frebel (2010); Norris et al. (2010); Ji et al. (2016b); Koch et al. (2013); Gilmore et al. (2013); Frebel, Simon & Kirby (2014); Ji et al. (2016a); Frebel et al. (2016); Kirby et al. (2017); Nagasawa et al. (2018); Ji et al. (2019); Marshall et al. (2019); Ji et al. (2020); Hansen et al. (2020); Waller et al. (2023); Chiti et al. (2023); Mardini, Frebel & Chiti (2023); Placco et al. (2023).

sample stars, it appears not unlikely that our sample stars formed from gas chemically enriched by a single supernova or explosive event only. Indeed, as been shown by Umeda & Nomoto (2002) and subsequent works, it is possible to reproduce the observations of extremely metal-poor stars (e.g. Cayrel et al. 2004) with the yields from just one massive energetic Pop III SN ('hypernova'), even when no elements with $Z > 30$ are considered. In the following, we discuss specific scenarios that may help explain the origins of the neutron-capture elements in all of our sample stars.

5.2 Neutron-capture nucleosynthesis processes

In the subsequent sections, we explore in more detail possible chemical enrichment scenarios for the [Sr/Ba] ratios observed in our sample stars, as seen in Fig. 6. But first, we note that about half of our sample stars likely formed from gas enriched by an *r*-process as indicated by their [Sr/Ba] ratios. This would imply that a neutron star merger or another massive stellar *r*-process source was responsible for the observed signatures (e.g. Lattimer & Schramm 1974; Symbalisty, Schramm & Wilson 1985; Eichler et al. 1989;

Table 6. MRL s-process predictions for metal-poor stars.

Ratio	Mean atomic number	[Fe/H] = −3.0 non-rotating	[Fe/H] = −4.0 non-rotating	[Fe/H] = −3.0 slow rotating	[Fe/H] = −4.0 slow rotating	[Fe/H] = −3.0 fast rotating	[Fe/H] = −4.0 fast rotating
[Sr/H]	87.7	− 6.47	− 8.68	− 4.57	− 5.62	−4.70	−5.72
[Y/H]	89.0	− 6.89	− 8.92	− 4.49	− 5.40	−4.43	−5.45
[Zr/H]	91.3	− 7.35	− 9.29	− 4.66	− 5.44	−4.41	−5.40
[Mo/H]	96.0	− 7.87	− 9.62	− 4.88	− 5.42	−4.60	−5.26
[Ba/H]	137.4	− 7.97	− 9.09	− 5.85	− 5.83	−4.61	−5.55
[Sr/Ba]		1.5	0.41	1.28	0.21	−0.09	−0.17

Notes. [a]Based on *s*-process yields in rotating massive low-metallicity stars presented in Pignatari et al. (2008). They indirectly give the rotation speed by the amount of ^{22}Ne produced through rotation-induced ^{14}N and available for the *s*-process. All values are calculated by assuming a dilution mass of 10^5 $M_\odot$, aC-shell mass of 3 $M_\odot$, and solar abundance from Asplund et al. (2009).

Siegel, Barnes & Metzger 2019; Siegel et al. 2022). The other half appears to be neutron-capture normal stars which may be the result of neutron-capture processes such as an *r*-process yield that was highly diluted in the surrounding gas, a limited *r*-process or an 'incomplete' *s*-process in massive stars. We discuss the latter two options in more detail below. Both these processes are associated with massive stars (possibly also the *r*-process) that would explode as type II SNe on short time-scales. This would provide fast enrichment across the early Universe and the original host systems of our metal-poor stars.

5.2.1 *Limited* r-*process in massive stars*

We only find two stars to be likely limited *r*-process stars, HE 2214 − 6127 and HE 2332 − 3039. Izutani, Umeda & Tominaga (2009) computed Sr, Y, and Zr yields of the weak/limited *r*-process. In order to reproduce observations of metal-poor stars with excesses in these lighter neutron-capture elements (compared to heavier ones) they find that massive 25 $M_\odot$ energetic hypernovae could be the sites of this process. They explore some of their model parameters and present results for a variation of ejected matter and electron fraction Y_e. Less massive, normal SNe appear to not produce enough light neutron-capture elements unless an extremely high entropy is assumed for the nucleosynthetic processing.

We employ the limited *r*-process yields from table 3 presented in Izutani, Umeda & Tominaga (2009) to calculate what the abundances of a metal-poor star would be assuming that it formed from material enriched by such a process. We calculate [Sr/H] ratios (we deliberately choose not to calculate values with respect to Fe as iron is produced completely independently of the neutron-capture elements). We assume that the Sr yields are mixed into a hydrogen cloud of 10^5 $M_\odot$ whose size is cosmologically motivated (see also Section 5.3).

The range in theoretical Sr yields leads to predictions for observed values of $-4.8 < [Sr/H] < -3.9$. Only few stars fall into this range. If we were to assume a slightly smaller gas mass, this range would become higher and could potentially explain the enrichment of HE 2214 − 6127 ([Sr/H] = −3.01) and HE 2332 − 3039 ([Sr/H] = −3.03), if physically realistic. We note that no yields are provided for heavier neutron-capture elements such as Ba.

5.2.2 s-*process in massive rotating low-metallicity stars*

To possibly explain the bulk of our stars stars (neutron-capture normal as well as stars currently classified as *r*-I; see overlap regions in Fig. 6) with their neutron-capture abundance that are neither significantly enhanced nor extraordinarily deficient, we consider the following enrichment scenario for early neutron-capture element production. Pignatari et al. (2008) calculated *s*-process nucleosynthesis occurring in massive, rotating low-metallicity ('MRL') stars. Stellar rotation induces mixing that has been shown to produce large amounts of ^{14}N in massive low-metallicity objects (Meynet, Ekström & Maeder 2006; Hirschi 2007). A fraction of this nitrogen is mixed in the He-burning core and converted to neon. This process provides free neutrons which are essential for the operation of the *s*-process. The amount of ^{22}Ne, however, is easily affected by the initial mass of the star, by the rotation speed as well as nuclear reaction rate uncertainties.

The massive non-rotation models of Pignatari et al. (2008) are extremely deficient of neutron-capture elements. But the *s*-process yields (e.g. Sr and Ba) for stars with [Fe/H] < −3.0 are orders of magnitudes higher in fast rotating 25 $M_\odot$ stars compared to non-rotating stars of the same mass. These drastic abundance changes are primarily dependent of the amount of available primary Ne nuclei. While the Sr production becomes saturated at high rotation speeds irrespective of the metallicity of the model, the Ba yields in the [Fe/H] = −3.0 model increase by more than 3 dex from the non-rotating to the rotating cases. For comparison, at solar metallicity, the weak-*s* process operates in massive stars also but it becomes very inefficient at low metallicity due to decreased amounts of required ^{22}Ne and Fe seeds (e.g. Prantzos, Hashimoto & Nomoto 1990). The MRL *s*-process yields are listed in Table 6.

We note that these yields are only those of the (secondary) *s*-process component. It neglects any contributions from the primary explosive component which entails a *p*-process component for which the incomplete *s*-process yields act as seed nuclei as well as any α-rich freezeout yields. These other components may add to the overall neutron-capture yields as presented in Pignatari et al. (2008) but likely not in large quantities (possibly a few tenths of a dex). Also, these calculations for a 25 $M_\odot$ are progenitor mass dependent, and for a more massive star the yields would linearly increase with stellar mass (Pignatari, private communication).

We utilize the yields of Pignatari et al. (2008), and again assume a 10^5 $M_\odot$ dilution mass, to calculate theoretical abundance levels for comparison with our observations. Based on values presented in Table 6, [Sr/H] abundances range from [Sr/H] < −5.7 to −4.6 dex for the rotating cases, as well as [Ba/H] < −5.9 to −4.6 dex. If anything, only CD −24°17504 broadly falls into these ranges, making it not unlikely that its neutron-capture elements were created in one single massive progenitor SN (see Section 5.3).

The theoretically predicted MRL [Sr/Ba] ratios are high (largely supersolar), ranging from $-0.17 < [Sr/Ba] < 1.28$, which agrees with values found for the bulk of our sample stars (see Fig. 6). This supports massive objects as progenitors for our observed stars. But again, assuming that early star forming gas masses may have

been limited, we can not exclude that [Sr/H] and [Ba/H] may each have been higher locally; the ratio would remain the same. For more context, we note that the [Sr/Ba] values found in the classical main-*s*-process stars[11] are much lower, [Sr/Ba] < -0.6. So are ratios produced by the main *r*-process, [Sr/Ba] ~ -0.4 to 0.4 dex as found in strongly *r*-process enriched stars.

Considering all the observations as well as the theoretical predictions for the MRL *s*-process it appears principally plausible that it was responsible for the chemical enrichment of the bulk of our sample stars, although the absolute yields would have needed to be distributed across a gas mass significantly smaller than 10^5 solar masses. Alternatively, we can conclude that principally any other process operating in massive stars would be able to explain the observed abundance ratios. These massive stars were most likely the earliest producers of any neutron-capture elements in the Universe. This would also be consistent with the extensive scatter in Sr abundances observed in metal-poor halo stars at the lowest metallicities (e.g. McWilliam et al. 1995; Aoki et al. 2005; Barklem et al. 2005; Francois et al. 2007; Roederer 2013; Frebel 2018).

5.3 Mono-enriched metal-poor stars

Motivated by the results found in Section 5.2, we further aim to define additional criteria that indicate whether a metal-poor star carries the nucleosynthetic signature of just one previous SN based on its Sr and Ba abundances. Hartwig et al. (2018) suggested a diagnostic tool (see their fig. 11) to identify 'mono-enriched stars' based on the observed [Mg/C] ratio at a given [Fe/H]. Unfortunately for our sample, carbon abundances could not be measured for all stars, which somewhat limits the use of this tool.

The upper panel of Fig. 7 shows [Mg/C] ratios as a function of [Fe/H] for our sample star with theoretically predicted contours from Hartwig et al. (2018). The blue dashed line represents the 3σ probability of a mono-enrichment origin. The red, yellow, and green dashed lines represent the 1σ, 2σ, and 3σ confidence intervals of the probability contours of multi-enrichment origins, respectively. The contours separate so it is possible to easily identify mono-enriched from multi-enriched stars in this diagram. We overplotted our sample stars using the same symbols in Fig. 5 and find that four (within error bars) out of the 15 stars (those with available carbon measurements) indeed most likely formed from gas chemically enriched by just one SN event (G64 − 12, CD −24°17504, HE 0232 − 3755, and HE 1245 − 0430). This corresponds to about 30 per cent of mono-enriched stars in our sample.

We then explored the possibility of the mono-enriched stars having unique [Sr/Ba] ratios that would make their identification more straightforward. We also wanted to check how this would map onto our earlier conclusions regarding single progenitors of our sample stars.

For that, we retrieved all JINAbase metal-poor stars with available C, Mg, Sr, and Ba abundance measurements. This selection yielded a sample of 1099 stars. We overplotted the observed [Mg/C] ratios as a function of [Fe/H] for this literature sample. 44 stars are mono-enriched, as seen in Fig. 7. In the bottom panel in Fig. 7, we then plot the two mono- and multi-enriched stellar populations in the [Sr/Ba] versus [Ba/Fe] diagram to investigate if there is a separation between the two populations. Filled triangles and circles represent the mono- and multi-enriched populations, respectively. Symbols are color-coded based on their [Fe/H] values. Representative measurements uncertainties are indicated by the error bar in each panel.

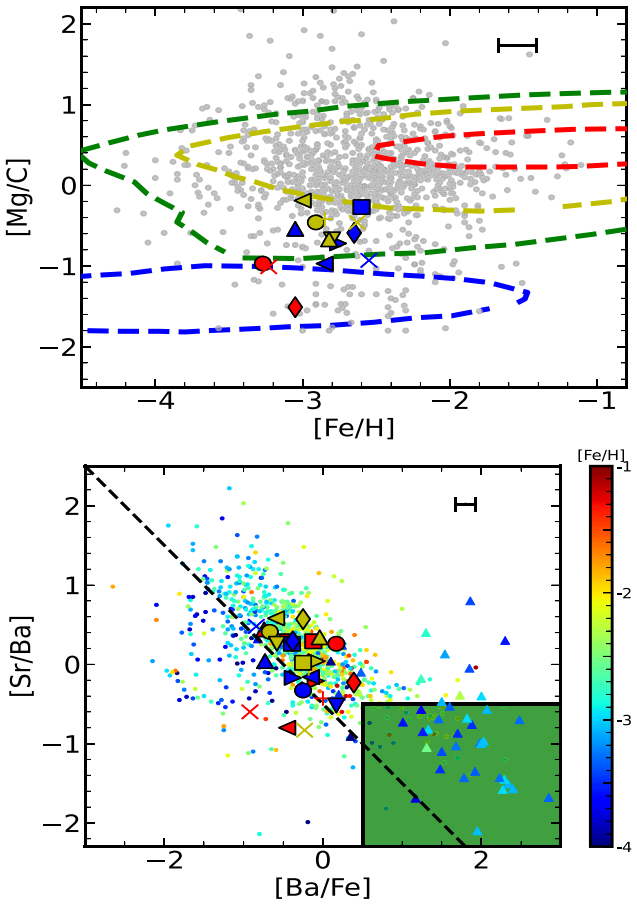

Figure 7. Upper panel shows the observed [Mg/C] ratios as a function of [Fe/H] for literature stars collected by JINAbase having C, Mg, Sr, and Ba measurements. The blue dashed line represents the 3σ probability of finding mono-enriched stars. The red, yellow, and green dashed lines represent the 1σ, 2σ, and 3σ of finding multiple-enriched stars, respectively. Bottom panel shows the distributions of the mono- (filled triangles) and multiple-enriched (filled circles) stars in the [Ba/Fe] versus [Sr/Ba] space, color-coded by their [Fe/H] values. Our sample stars are overplotted using same symbols as in Fig. 5. A clear separation between the mono- and multi-enriched stars can not be drawn in the [Ba/Fe] versus [Sr/Ba] space. However, a considerable fraction of the mono-enriched stars seem to populate the shaded region which is defined by [Ba/Fe] >1.0, [Sr/Ba] <-0.5, and [Fe/H] <-2.7. Our mono-enriched stars reside outside the green shaded region as they have [Ba/Fe] <1.0. Dashed-line denotes [Sr/Ba] $=-$ [Ba/Fe] $- 0.50$ as used in Fig. 5. Representative measurements uncertainties are indicated by the error bar in each panel.

The two populations seem to be overlapping in the [Sr/Ba]–[Ba/Fe] diagram. However, a considerable number of mono-enriched metal-poor stars are preferentially located at [Ba/Fe] > 0.5, [Sr/Ba] <-0.5, and [Fe/H] <-2.7 in the figure (the green shaded area). Unfortunately, non of our sample stars reside within that region. In general, it seems that the [Sr/Ba]-[Ba/Fe] space is not very helpful for making robust conclusion on the number of the SN events responsible for the chemical enrichment of our target stars. Therefore, we hold on our results found using the [Mg/C] versus [Fe/H] space.

[11] Those stars are in binary systems and only occur with metallicities of [Fe/H] $\gtrsim -2.6$. They are not further considered here.

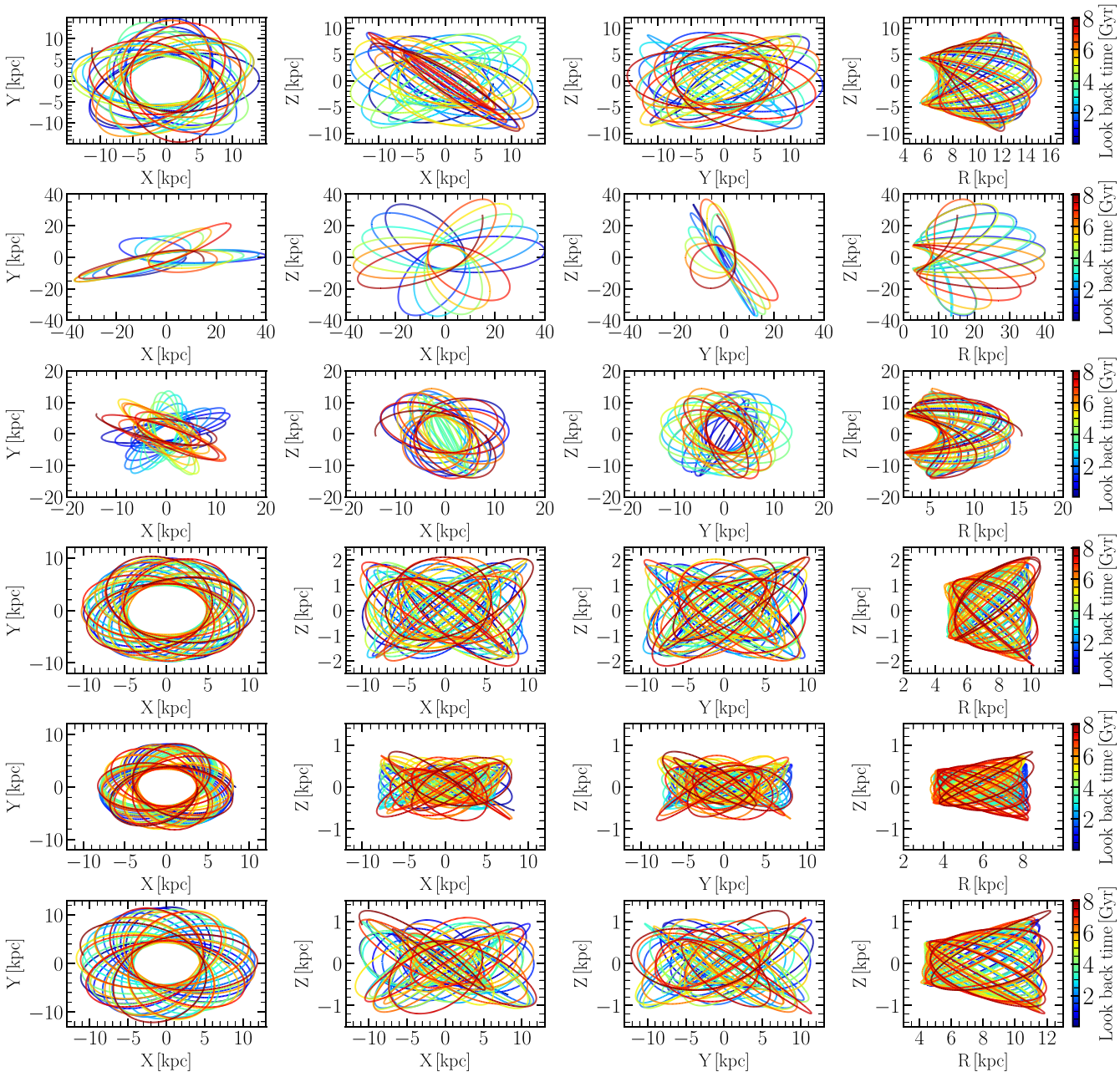

Figure 8. Halo star orbital histories for CS 30302-145 (first row), and CD −24°17504 (second row), and HE 2045 − 5057 (third row). Disk star orbital histories for HE 2133 − 0421 (fourth row), HE 0223 − 2814 (fifth row), and CS 29504-018 (sixth row).

5.4 Kinematic and orbital properties of the star sample

Adding orbital information to chemical abundance analysis results can be helpful to further identify the origins of the observed element signatures (e.g. Mardini et al. 2022a, b). Therefore, we investigated the dynamical origins of our sample stars. We retrieved the proper motions ($\mu_\alpha \cos\delta$, μ_δ) and parallaxes (ϖ) from Gaia EDR3 (Gaia Collaboration 2021). We adopted the line-of-sight velocities (V_r) reported in Table 1. We corrected ϖ as suggested in Lindegren et al. (2021) and derived heliocentric distances using an exponentially decreasing space density prior as presented in Mardini et al. (2022b). With these quantities we can construct the full space motions of our sample.

We assume that the Sun is located at $R_\odot = 8.178 \pm 0.013$ kpc from the Galactic centre (Gravity Collaboration 2019), $z_\odot = 20.8 \pm 0.3$ pc above the Galactic plane, and has peculiar motion $U_\odot = 11.1 \pm 0.72$ km s^{-1} (Bennett & Bovy 2019), $V_\odot = 12.24 \pm 0.47$ km s^{-1}, and $W_\odot = 7.25 \pm 0.36$ km s^{-1} (Schönrich, Binney & Dehnen 2010). We take $V_{LSR} = 220$ km s^{-1} (Kerr & Lynden-Bell 1986). We used `The-ORIENT`[12] [for more details, we refer the readers to Mardini et al. (2020, 2022a)] to integrate the corresponding stellar orbits, apocentric (r_{apo}) and pericentric (r_{peri}) radii, the maximum offset from the Galactic midplane (Z_{max}), and eccentricity, defined as $e = (r_{apo} - r_{peri})/(r_{apo} + r_{peri})$.

[12] https://github.com/Mohammad-Mardini/The-ORIENT.

Table 7. Calculated orbital parameters, energies, stellar actions, and membership.

Star	r_{apo} (kpc)	r_{peri} (kpc)	Z_{max} (kpc)	e	E (10^5 km^2 s^{-1})	L_z (kpc km s^{-1})	J_r (kpc km s^{-1})	J_z (kpc km s^{-1})	Membership
CD −24°17504	17.82	6.84	16.29	0.45	−0.74	286.95	1319.59	− 695.73	SASS
CS22188 − 033	8.38	0.66	0.74	0.85	−1.14	558.33	11.42	− 155.12	Halo
CS29504 − 018	14.49	4.25	1.23	0.55	−0.85	418.39	14.40	1606.42	Thin disc
CS29519 − 133	9.29	2.22	1.14	0.61	−1.06	347.47	22.77	− 712.32	Halo
CS30302 − 145	20.02	6.93	5.88	0.49	−0.71	442.30	134.61	− 2006.06	SASS
G64 − 12	100.47	8.07	92.98	0.85	−0.25	4801.88	2329.85	− 1114.11	Halo
HE 0219 − 2056	16.15	0.35	2.74	0.96	−0.85	1195.22	58.88	269.97	Halo
HE 0223 − 2814	8.79	3.46	0.58	0.44	−1.04	183.17	8.27	1237.36	Thin disc
HE 0232 − 3755	36.32	6.33	35.27	0.70	−0.53	1390.51	2023.68	489.77	Halo
HE 0406 − 3120	22.18	2.34	3.19	0.81	−0.72	1226.91	33.08	1136.49	Halo
HE 0526 − 4059	15.05	1.06	10.26	0.87	−0.87	907.17	276.35	− 202.14	Halo
HE 1200 − 0009	33.36	5.32	17.37	0.72	−0.56	1410.04	498.31	− 1479.53	Halo
HE 1214 − 1050	9.00	4.04	3.29	0.38	−1.00	138.08	138.73	− 992.80	Halo
HE 1245 − 0430	15.39	7.68	11.95	0.33	−0.77	167.03	851.93	1390.80	Halo
HE 1309 − 1113	12.39	4.92	10.51	0.43	−0.87	217.58	784.41	− 635.18	Halo
HE 1401 − 0010	39.84	5.52	39.84	0.76	−0.51	1760.81	2204.47	98.21	Halo
HE 1436 − 0654	7.66	0.99	1.18	0.77	−1.17	410.40	32.25	477.74	Atari
HE 1929 − 6715	7.91	5.57	0.41	0.17	−1.01	30.95	5.42	− 1358.20	Halo
HE 2045 − 5057	9.69	2.58	0.86	0.58	−1.03	326.59	15.63	1032.78	SASS
HE 2130 − 4852	26.49	2.53	6.74	0.83	−0.66	1469.76	90.64	1157.52	Halo
HE 2133 − 0421	10.02	5.50	1.74	0.29	−0.94	96.95	43.97	1604.92	Atari
HE 2141 − 2916	7.20	1.40	6.08	0.67	−1.13	233.97	413.95	311.72	Halo
HE 2214 − 6127	8.31	4.10	7.71	0.34	−1.01	84.19	811.98	− 289.46	Halo
HE 2308 − 3543	12.64	0.63	4.83	0.91	−0.95	872.71	68.33	331.39	Halo
HE 2332 − 3039	8.12	0.36	0.92	0.91	−1.16	581.89	14.98	250.92	Halo

Employing our action-velocity separation tool developed by Mardini et al. (2022b), we assign individual stars to one of the various Galactic components (thin disc, thick disc, and halo). In brief, this tool utilizes the space velocities distributions and stellar action probability distribution functions of each of the Galactic components to calculate the relative likelihood for a given star of being a member of a specific Galactic population (see equations 3, 5, 6, and 7 in Mardini et al. 2022b).

We find that all of our stars belong to the Galactic halo except CS 29504-018, HE 0223 − 2814, and HE 2133 − 0421 which have disc-like kinematics. Fig. 8 shows the orbital histories of several example stars. The outer halo-like nature for CS 30302-145 (first row), CD −24°17504 (second row), and HE 2045 − 5057 (third row) is clearly seen. So is the disc-like nature of HE 2133 − 0421 (fourth row), HE 0223 − 2814 (fifth row), and CS 29504-018 (sixth row).

For the three disc-like kinematics stars, only one has a C measurement which indicates HE 2133 − 0421 to be a multi-enriched star. This aligns with it residing in the disc now and (likely) having formed in the disc where multiple SNe would have contributed to the enrichment of the birth cloud, with the disc having a high star formation rate. For the 24 halo-like kinematics stars (14 of which have C abundances), four (G64 − 12, CD −24°17504, HE 0232 − 3755, and HE 1245 − 0430) stars are mono-enriched and 10 are multi-enriched.

The orbital histories for the stars (CS 30302-145, CD −24°17504, and HE 2045 − 5057) that reside in the UFDs region (see Fig. 6, as these all have the lowest [Sr/Fe] values) indicate an outer-halo kinematic. This adds additional line of evidence for the mono-enrichment scenario of CD −24°17504. Also, the extremely low Sr and Ba abundances derived for CD −24°17504 suggests that it could have originated in a satellite galaxy similar to the ones that survived to the present day. In Andales et al. (2023), we further investigated low Sr stars as they are the most likely stars that originated in small dwarf galaxies that got accreted in the earliest phase(s) of the history of the Galaxy. The criterion for a star from a 'small accreted stellar system' (SASS), is [Sr/H] < −4.5. With [Sr/H] = −4.75 and [Ba/H] = −4.15, CD −24°17504 fulfills this criterion, making it an ancient SASS star from the early Universe. Therefore, it is most likely that CD −24°17504 is one of the first Pop II stars to have formed – before or during the early formation phase of the Milky Way.

6 CONCLUSIONS AND SUMMARY

We have presented a chemo-dynamical analysis of twenty seven metal-poor main-sequence stars with [Fe/H] <−2.5. These stars were chosen from the program that selects metal-poor candidates (Christlieb et al. 2008) from the Hamburg/ESO objective-prism survey (Wisotzki et al. 1996). The high-resolution observations were obtained using the MIKE spectrograph on the *Magellan-Clay* telescope at Las Campanas Observatory, for which 20 stars were followed-up, for the first time.

We derived chemical abundances for 17 elements for our stars. The mean Li abundance ($\langle A(\mathrm{Li})\rangle = 2.13$) for our sample is in good agreement with values found in other dwarfs at the 'Spite plateau'. We measured carbon abundances for 15 stars, of which 12 are carbon-enhanced metal-poor stars ([C/Fe] >0.7). In general, the light element ($Z < 30$) abundances do not differ significantly from those of other similarly metal-poor halo main-sequence stars or giants (see Fig. 5), which points to a universal enrichment history of the birth environment(s). Of the heavy elements, we were only able to measure abundances for Sr and Ba which principally agree with those of literature metal-poor stars.

We further investigated the origins of the neutron-capture elements. We started with the available metal-poor stars data collected by JINAbase, UFDs stars, and abundance criteria from Frebel (2018) for identifying different heavy element nucleosynthesis signatures.

The observed [Sr/Ba] ratios for the vast majority of our sample are located in regions in the [Sr/Ba] versus [Ba/Fe] space typically occupied by *r*-I and neutron-capture normal stars, as depicted in Fig. 6. For example, two stars, HE 2214 − 6127 and HE 2332 − 3039, have [Sr/H] values roughly in agreement with what is predicted by the limited *r*-process yields presented in Izutani, Umeda & Tominaga (2009). The predicted yields of the 'incomplete' *s*-process presented in Pignatari et al. (2008) broadly matches several stars, but primarily in their [Sr/Ba] ratios. The overall low [Sr/H] and [Ba/H] values are not inconsistent with those of CD −24°17504 but not ideal match exists when assuming a gas mixing mass of 10^5 $M_\odot$.

Therefore, we conclude that, most likely, the bulk of our stars formed from early gas clouds enriched by either an *r*-process event (e.g. neutron star merger), a limited *r*-process, or an 'incomplete' *s*-process in massive stars. All these processes have the potential to leave behind signatures that results in observed abundance patterns associated with *r*-I and neutron-capture normal stars. It remains to be seen whether fast enrichment by SNe dominated these enrichment levels among the original host systems of our stars, or whether later time enrichment by neutron star mergers occurred in some ways before our metal-poor stars formed. Finally, HE 0232 − 3755 is most likely an *r*-II star as its [Sr/Ba] ratio can be explained by an *r*-process event.

We also performed a full orbital history analysis of our sample stars, using astrometric data from Gaia EDR3 (Gaia Collaboration 2021). This analysis suggests halo-like kinematics for the vast majority of our sample. This points to an accretion origin of these stars. Finally, we used [Mg/C] versus [Fe/H] criterion by Hartwig et al. (2018) to identify mono-enriched stars in our sample, i.e. stars with just one progenitor. Based on the observed ratios, about 30 per cent of our sample stars with carbon measurements appear to be mono-enriched and likely formed from gas clouds enriched by just one previous SN. This contrasts the kinematic signature of HE 2133 − 0421, HE 0223 − 2814, and CS 29504-018 which are clearly disc-like in nature.

Then there are are several interesting stars to mention. Three stars, CS 30302-145, HE 2045 − 5057, and CD −24°17504, have [Sr/Ba] and [Ba/Fe] ratios consistent with those observed in typical UFDs stars. They also all have halo-like kinematics. This strongly suggests that they originated in long-disrupted early dwarf galaxies. Of particular interest in this context is CD −24°17504 which has the lowest Sr and Ba abundances in our sample. Its distinct chemodynamical nature is consistent with an origin in a SASS that was absorbed by the proto-Milky Way, as laid out in Andales et al. (2023). This suggest that CD −24°17504 is likely among the earliest, and hence oldest, Pop II stars to have formed in the Universe. More stars with low Sr and Ba abundance measurements will help to identify more of these ancient survivors from the early universe.

ACKNOWLEDGEMENTS

This work was initiated at an event supported by the National Science Foundation under Grant No. PHY-1430152 (JINA Center for the Evolution of the Elements).' MKM acknowledges support from NSF grant OISE 1927130 (International Research Network for Nuclear Astrophysics/IReNA). AF acknowledges support from NSF CAREER grants AST-1255160, NSF grant AST-1716251, and NSF grant AST-2307436. This work made use of the NASA's Astrophysics Data System Bibliographic Services. This work has made use of data from the European Space Agency (ESA) mission *Gaia* (https://www.cosmos.esa.int/gaia), processed by the *Gaia* Data Processing and Analysis Consortium (DPAC, https://www.cosmos.esa.int/web/gaia/dpac/consortium). Funding for the DPAC has been provided by national institutions, in particular the institutions participating in the *Gaia* Multilateral Agreement. This research has made use of the SIMBAD database, operated at CDS, Strasbourg, France.

This paper includes data gathered with the 6.5-m *Magellan Telescopes* located at Las Campanas Observatory, Chile.

DATA AVAILABILITY

The data underlying this article will be shared upon reasonable request to the corresponding author.

REFERENCES

Abohalima A., Frebel A., 2018, ApJS, 238, 36
Aguado D. S. et al., 2021, MNRAS, 500, 889
Aguado D. S., Allende Prieto C., González Hernández J. I., Rebolo R., 2018, ApJ, 854, L34
Aguado D. S., Allende Prieto C., González Hernández J. I., Rebolo R., Caffau E., 2017a, A&A, 604, A9
Aguado D. S., González Hernández J. I., Allende Prieto C., Rebolo R., 2017b, A&A, 605, A40
Almusleh N. A., Taani A., Özdemir S., Rah M., Al-Wardat M. A., Zhao G., Mardini M. K., 2021, Astron. Nachr., 342, 625
Amarsi A. M., Lind K., Asplund M., Barklem P. S., Collet R., 2016, MNRAS, 463, 1518
Andales H. D., Figueiredo A. S., Fienberg C. G., Mardini M. K., Frebel A., 2023, MNRAS
Aoki W. et al., 2005, ApJ, 632, 611
Aoki W. et al., 2013, AJ, 145, 13
Aoki W., Beers T. C., Christlieb N., Norris J. E., Ryan S. G., Tsangarides S., 2007, ApJ, 655, 492
Aoki W., Norris J. E., Ryan S. G., Beers T. C., Ando H., 2002, ApJ, 576, L141
Asplund M., Grevesse N., Sauval A. J., Scott P., 2009, ARA&A, 47, 481
Barklem P. S. et al., 2005, A&A, 439, 129
Beers T. C., Rossi S., Norris J. E., Ryan S. G., Shefler T., 1999, AJ, 117, 981
Behara N. T., Bonifacio P., Ludwig H. G., Sbordone L., González Hernández J. I., Caffau E., 2010, A&A, 513, A72
Belokurov V., Erkal D., Evans N. W., Koposov S. E., Deason A. J., 2018, MNRAS, 478, 611
Bennett M., Bovy J., 2019, MNRAS, 482, 1417
Bernstein R., Shectman S. A., Gunnels S. M., Mochnacki S., Athey A. E., 2003, in Iye M., Moorwood A. F. M., eds, Proc. SPIE Conf. Ser. Vol. 4841, Instrument Design and Performance for Optical/Infrared Ground-based Telescopes. SPIE, US, p. 1694
Bonifacio P. et al., 2007, A&A, 462, 851
Bonifacio P. et al., 2009, A&A, 501, 519
Bonifacio P., Sbordone L., Caffau E., Ludwig H. G., Spite M., González Hernández J. I., Behara N. T., 2012, A&A, 542, A87
Bromm V., Coppi P. S., Larson R. B., 2002, ApJ, 564, 23
Bromm V., Yoshida N., 2011, ARA&A, 49, 373
Caffau E. et al., 2011a, Nature, 477, 67
Caffau E. et al., 2011b, A&A, 534, A4
Caffau E. et al., 2013, A&A, 560, A15
Carney B. W., Peterson R. C., 1981, ApJ, 245, 238
Carretta E., Gratton R., Cohen J. G., Beers T. C., Christlieb N., 2002, AJ, 124, 481
Casagrande L., VandenBerg D. A., 2018a, MNRAS, 475, 5023
Casagrande L., VandenBerg D. A., 2018b, MNRAS, 479, L102
Casey A. R., 2014, PhD thesis, Australian National University, Canberra
Casey A. R., Schlaufman K. C., 2015, ApJ, 809, 110
Cayrel R. et al., 2004, A&A, 416, 1117
Cayrel R., 1996, A&AR, 7, 217

Chan C., Heger A., 2017, in Kubono S., Kajino T., Nishimura S., Isobe T., Nagataki S., Shima T., Takeda Y., eds, 14th International Symposium on Nuclei in the Cosmos (NIC2016). p. 20209
Chiti A. et al., 2023, AJ, 165, 55
Chiti A., Mardini M. K., Frebel A., Daniel T., 2021, ApJ, 911, L23
Christlieb N. et al., 2002, Nature, 419, 904
Christlieb N., Schörck T., Frebel A., Beers T. C., Wisotzki L., Reimers D., 2008, A&A, 484, 721
Cohen J. G. et al., 2004, ApJ, 612, 1107
Cohen J. G., Christlieb N., Thompson I., McWilliam A., Shectman S., Reimers D., Wisotzki L., Kirby E., 2013, ApJ, 778, 56
Deliyannis C. P., Demarque P., Kawaler S. D., 1990, ApJS, 73, 21
Depagne E., Hill V., Christlieb N., Primas F., 2000, A&A, 364, L6
Dotter A., Chaboyer B., Jevremović D., Kostov V., Baron E., Ferguson J. W., 2008, ApJS, 178, 89
Eichler D., Livio M., Piran T., Schramm D. N., 1989, Nature, 340, 126
Ezzeddine R. et al., 2019, ApJ, 876, 97
For B.-Q., Sneden C., 2010, AJ, 140, 1694
Francois P. et al., 2007, A&A, 476, 935
Frebel A. et al., 2005, Nature, 434, 871
Frebel A., 2010, Astron. Nachr., 331, 474
Frebel A., 2018, Annu. Rev. Nucl. Part. Sci., 68, 237
Frebel A., Casey A. R., Jacobson H. R., Yu Q., 2013, ApJ, 769, 57
Frebel A., Chiti A., Ji A., Jacobson H. R., Placco V., 2015, ApJL, 810, L27
Frebel A., Collet R., Eriksson K., Christlieb N., Aoki W., 2008, ApJ, 684, 588
Frebel A., Ji A. P., Ezzeddine R., Hansen T. T., Chiti A., Thompson I. B., Merle T., 2019, ApJ, 871, 146
Frebel A., Johnson J. L., Bromm V., 2007a, MNRAS, 380, L40
Frebel A., Norris J. E., Aoki W., Honda S., Bessell M. S., Takada-Hidai M., Beers T. C., Christlieb N., 2007b, ApJ, 658, 534
Frebel A., Norris J. E., 2015, ARA&A, 53, 631
Frebel A., Norris J. E., Gilmore G., Wyse R. F. G., 2016, ApJ, 826, 110
Frebel A., Simon J. D., Geha M., Willman B., 2010, ApJ, 708, 560
Frebel A., Simon J. D., Kirby E. N., 2014, ApJ, 786, 74
Gaia Collaboration, 2016, A&A, 595, A1
Gaia Collaboration, 2021, A&A, 649, A1
Gaia Collaboration, 2023, A&A, 674, A1
Gilmore G., Norris J. E., Monaco L., Yong D., Wyse R. F. G., Geisler D., 2013, ApJ, 763, 61
Giribaldi R. E., da Silva A. R., Smiljanic R., Cornejo Espinoza D., 2021, A&A, 650, A194
Gravity Collaboration, 2019, A&A, 625, L10
Greif T. H., Johnson J. L., Klessen R. S., Bromm V., 2008, MNRAS, 387, 1021
Gull M., Frebel A., Hinojosa K., Roederer I. U., Ji A. P., Brauer K., 2021, ApJ, 912, 52
Hansen T. et al., 2015, ApJ, 807, 173
Hansen T. T. et al., 2020, ApJ, 897, 183
Hartwig T. et al., 2018, MNRAS, 478, 1795
Helmi A., 2020, ARA&A, 58, 205
Helmi A., Babusiaux C., Koppelman H. H., Massari D., Veljanoski J., Brown A. G. A., 2018, Nature, 563, 85
Hirschi R., 2007, A&A, 461, 571
Hollek J. K., Frebel A., Roederer I. U., Sneden C., Shetrone M., Beers T. C., Kang S.-j., Thom C., 2011, ApJ, 742, 54
Honda S., Aoki W., Beers T. C., Takada-Hidai M., 2011, ApJ, 730, 77
Hong J. et al., 2023, preprint (arXiv:2311.02297)
Ishigaki M. N., Chiba M., Aoki W., 2012, ApJ, 753, 64
Izutani N., Umeda H., Tominaga N., 2009, ApJ, 692, 1517
Jacobson H. R. et al., 2015, ApJ, 807, 171
Ji A. P. et al., 2020, ApJ, 889, 27
Ji A. P., Frebel A., Bromm V., 2014, ApJ, 782, 95
Ji A. P., Frebel A., Chiti A., Simon J. D., 2016a, Nature, 531, 610
Ji A. P., Frebel A., Simon J. D., Geha M., 2016b, ApJ, 817, 41
Ji A. P., Simon J. D., Frebel A., Venn K. A., Hansen T. T., 2019, ApJ, 870, 83
Keller S. C. et al., 2014, Nature, 506, 463
Kelson D. D., 2003, PASP, 115, 688
Kerr F. J., Lynden-Bell D., 1986, MNRAS, 221, 1023
Kirby E. N., Cohen J. G., Simon J. D., Guhathakurta P., Thygesen A. O., Duggan G. E., 2017, ApJ, 838, 83
Kobayashi C., Ishigaki M. N., Tominaga N., Nomoto K., 2014, ApJ, 785, L5
Koch A., Feltzing S., Adén D., Matteucci F., 2013, A&A, 554, A5
Koch A., McWilliam A., Grebel E. K., Zucker D. B., Belokurov V., 2008, ApJL, 688, L13
Kurucz R., 1993, ATLAS9 Stellar Atmosphere Programs and 2 km/s grid. Kurucz CD-ROM No. 13. Cambridge. p. 13
Lai D. K., Bolte M., Johnson J. A., Lucatello S., 2004, AJ, 128, 2402
Lai D. K., Bolte M., Johnson J. A., Lucatello S., Heger A., Woosley S. E., 2008, ApJ, 681, 1524
Latham D. W., Stefanik R. P., Torres G., Davis R. J., Mazeh T., Carney B. W., Laird J. B., Morse J. A., 2002, AJ, 124, 1144
Lattimer J. M., Schramm D. N., 1974, ApJ, 192, L145
Li H.-N., Aoki W., Honda S., Zhao G., Christlieb N., Suda T., 2015a, Res. Astron. Astrophys., 15, 1264
Li H., Aoki W., Zhao G., Honda S., Christlieb N., Suda T., 2015b, PASJ, 67, 84
Li H.-N., Zhao G., Christlieb N., Wang L., Wang W., Zhang Y., Hou Y., Yuan H., 2015c, ApJ, 798, 110
Lindegren L. et al., 2021, A&A, 649, A4
Mardini M. K. et al., 2019a, ApJ, 875, 89
Mardini M. K., Placco V. M., Taani A., Li H., Zhao G., 2019b, ApJ, 882, 27
Mardini M. K., Ershiadat N., Al-Wardat M. A., Taani A. A., Özdemir S., Al-Naimiy H., Khasawneh A., 2019c, J. Phys.: Conf. Ser., 1258, 012024
Mardini M. K. et al., 2020, ApJ, 903, 88
Mardini M. K. et al., 2022a, MNRAS, 517, 3993
Mardini M. K., Frebel A., Chiti A., Meiron Y., Brauer K. V., Ou X., 2022b, ApJ, 936, 78
Mardini M. K., Frebel A., Chiti A., 2023, MNRASL, available at: https://doi.org/10.1093/mnrasl/slad197
Marshall J. L. et al., 2019, ApJ, 882, 177
Masseron T. et al., 2006, A&A, 455, 1059
Matsuno T., Aoki W., Beers T. C., Lee Y. S., Honda S., 2017, AJ, 154, 52
McWilliam A., Preston G. W., Sneden C., Searle L., 1995, AJ, 109, 2757
Meyer B. S., 1994, ARA&A, 32, 153
Meynet G., Ekström S., Maeder A., 2006, A&A, 447, 623
Mucciarelli A., Bellazzini M., Massari D., 2021, A&A, 653, A90
Nagasawa D. Q. et al., 2018, ApJ, 852, 99
Norris J. E. et al., 2013, ApJ, 762, 25
Norris J. E., Christlieb N., Korn A. J., Eriksson K., Bessell M. S., Beers T. C., Wisotzki L., Reimers D., 2007, ApJ, 670, 774
Norris J. E., Ryan S. G., Beers T. C., 2001, ApJ, 561, 1034
Norris J. E., Yong D., Frebel A., Ryan S. G., 2023, MNRAS, 522, 1358
Norris J. E., Yong D., Gilmore G., Wyse R. F. G., 2010, ApJ, 711, 350
Pignatari M., Gallino R., Meynet G., Hirschi R., Herwig F., Wiescher M., 2008, ApJL, 687, L95
Placco V. M., Frebel A., Beers T. C., Christlieb N., Lee Y. S., Kennedy C. R., Rossi S., Santucci R. M., 2014a, ApJ, 781, 40
Placco V. M. et al., 2014b, ApJ, 790, 34
Placco V. M. et al., 2020, ApJ, 897, 78
Placco V. M. et al., 2023, ApJ, 959, 60
Placco V. M., Beers T. C., Reggiani H., Meléndez J., 2016, ApJ, 829, L24
Placco V. M., Frebel A., Beers T. C., Karakas A. I., Kennedy C. R., Rossi S., Christlieb N., Stancliffe R. J., 2013, ApJ, 770, 104
Placco V. M., Frebel A., Lee Y. S., Jacobson H. R., Beers T. C., Pena J. M., Chan C., Heger A., 2015, ApJ, 809, 136
Plez B., Cohen J. G., 2005, A&A, 434, 1117
Prantzos N., Abia C., Cristallo S., Limongi M., Chieffi A., 2020, MNRAS, 491, 1832
Prantzos N., Hashimoto M., Nomoto K., 1990, A&A, 234, 211
Rich J. A., Boesgaard A. M., 2009, ApJ, 701, 1519
Riello M. et al., 2021, A&A, 649, A3
Roederer I. U., 2013, ApJS, 145, 26
Roederer I. U., Preston G. W., Thompson I. B., Shectman S. A., Sneden C., Burley G. S., Kelson D. D., 2014a, AJ, 147, 136

Roederer I. U., Jacobson H. R., Thanathibodee T., Frebel A., Toller E., 2014b, ApJ, 797, 69
Ryan S. G., Norris J. E., Beers T. C., 1996, ApJ, 471, 254
Ryan S. G., Norris J. E., Beers T. C., 1999, ApJ, 523, 654
Ryan S. G., Norris J. E., Bessell M. S., 1991, AJ, 102, 303
Schneider R., Omukai K., Limongi M., Ferrara A., Salvaterra R., Chieffi A., Bianchi S., 2012, MNRAS, 423, L60
Schönrich R., Binney J., Dehnen W., 2010, MNRAS, 403, 1829
Siegel D. M., Agarwal A., Barnes J., Metzger B. D., Renzo M., Villar V. A., 2022, ApJ, 941, 100
Siegel D. M., Barnes J., Metzger B. D., 2019, Nature, 569, 241
Simon J. D., Frebel A., McWilliam A., Kirby E. N., Thompson I. B., 2010, ApJ, 716, 446
Sivarani T. et al., 2006, A&A, 459, 125
Sneden C. A., 1973, PhD thesis, The University of Texas, Austin
Sneden C., Cowan J. J., Gallino R., 2008, ARA&A, 46, 241
Sobeck J. S. et al., 2011, AJ, 141, 175
Spite F., Spite M., 1982, A&A, 115, 357
Spite M., Depagne E., Nordström B., Hill V., Cayrel R., Spite F., Beers T. C., 2000, A&A, 360, 1077
Spite M., Spite F., Bonifacio P., Caffau E., François P., Sbordone L., 2014, A&A, 571, A40
Spite M., Spite F., Cayrel R., Hill V., Nordström B., Barbuy B., Beers T., Nissen P. E., 1999, Ap&SS, 265, 141
Susmitha Rani A., Sivarani T., Beers T. C., Fleming S., Mahadevan S., Ge J., 2016, MNRAS, 458, 2648
Symbalisty E. M. D., Schramm D. N., Wilson J. R., 1985, ApJ, 291, L11
Taani A., Karino S., Song L., Al-Wardat M., Khasawneh A., Mardini M. K., 2019a, Res. Astron. Astrophys., 19, 012
Taani A., Abushattal A., Mardini M. K., 2019b, Astron. Nachr., 340, 847
Taani A., Vallejo J. C., Abu-Saleem M., 2022, J. High Energy Astrophys., 35, 83
Travaglio C., Gallino R., Arnone E., Cowan J., Jordan F., Sneden C., 2004, ApJ, 601, 864
Truran J. W., Cowan J. J., Pilachowski C. A., Sneden C., 2002, PASP, 114, 1293
Umeda H., Nomoto K., 2002, ApJ, 565, 385
Waller F. et al., 2023, MNRAS, 519, 1349
Wanajo S., Ishimaru Y., 2005, in Hill V., Francois P., Primas F., eds, IAU Symposium Vol. 228, From Lithium to Uranium: Elemental Tracers of Early Cosmic Evolution. Cambridge Univ. Press, Cambridge, p. 435
Wanajo S., Kajino T., Mathews G. J., Otsuki K., 2001, ApJ, 554, 578
Wise J. H., Turk M. J., Norman M. L., Abel T., 2012, ApJ, 745, 50
Wisotzki L., Koehler T., Groote D., Reimers D., 1996, A&AS, 115, 227
Woosley S. E., Weaver T. A., 1995, ApJS, 101, 181
Yong D. et al., 2013, ApJ, 762, 26

SUPPORTING INFORMATION

Supplementary data are available at *MNRAS* online.

Table 2. *Magellan*/MIKE abundances.
Table 4. *Magellan*/MIKE abundances.

Please note: Oxford University Press is not responsible for the content or functionality of any supporting materials supplied by the authors. Any queries (other than missing material) should be directed to the corresponding author for the article.

This paper has been typeset from a TEX/LATEX file prepared by the author.